

**DTIC**  
**S** ELECTE  
JAN 06 1994  
**A**

**AD-A274 414**  
|||||

2

# **An Experimental Study of Plunging Liquid Jet Induced Air Carryunder and Dispersion**

## **FINAL REPORT**

12-17-93

R.T. Lahey, Jr. (CoPI), D.A. Drew (CoPI)

*Center for Multiphase Research*

*Rensselaer Polytechnic Institute*

*Troy, NY 12180-3590 USA*

*N00014-91-J-1271*

**CMR**  
**CMR**  
**CMR**

## **ABSTRACT**

This report is divided into four parts: Part-I provides an introduction to plunging jet phenomena and summarizes the major findings of our previous research. Part-II presents a summary of the major experimental findings obtained during at Rensselaer. Part-III describes two proposed mechanisms responsible for air entrainment. Part-IV presents the results of two different numerical calculations, one using a Euler-Lagrangian approach and the other based on solving a full two-fluid model with a CFD code. Finally Part-V gives conclusions and recommendations for future research.

## **PART-I: INTRODUCTION**

The gas entrained by a plunging liquid jet and the resultant two-phase jet dispersion occur in many problems of practical interest. In particular, the air entrainment process due to the breaking bow waves of surface ships may cause long (ie, up to 5 km in length) wakes. Naturally easily detectable wakes are undesirable for naval warships. The ecological balance in lakes and oceans is also dependent on the amount of dissolved oxygen. A good understanding of the air carryunder and bubble dispersion process associated with a plunging liquid jet is vital if one is to be able to quantify such diverse phenomena as sea surface chemistry, the meteorological significance of (breaking) ocean waves, the

This document has been approved  
for public release and sale; its  
distribution is unlimited.

**93 12 22 2 34**

**93-31133**

|||||

7196

performance of certain type of chemical reactors, the "greenhouse" effect (ie, the absorption of CO<sub>2</sub> by the oceans), and a number of other important maritime-related applications. Significantly the absorption of greenhouse gases into the ocean has been hypothesized to be highly dependent upon the air carryunder that occurs due to breaking waves. This process can be approximated with a plunging liquid jet (Monahan [1991], Kerman [1984]). In addition, the air carryunder that occurs at most hydraulic structures in rivers is primarily responsible for the large air/water mass transfer that is associated with these structures (Avery and Novak [1978]).

Also, air entrainment plays an important role in slug flow phenomena in conduits. Indeed the liquid film surrounding the Taylor bubble has a mean flow in the opposite direction from the Taylor bubble. This liquid forms a type of plunging jet that produces a surface depression in the rear part of the Taylor bubble. When the annular liquid jet exceeds a critical velocity, the plunging liquid jet entrains into the liquid slugs small bubbles from the air in the Taylor bubble. These bubbles follow and may coalesce with the Taylor bubbles .

A number of prior studies have been performed in which axisymmetric plunging liquid jets have been used to investigate the air carryunder process. These include the work of Lin & Donnelly [1966], Burgess et al [1972], Van De Sande & Smith [1973], Koga [1982], McKeogh & Ervine [1981], and Detsch & Sharma [1991], Ohkawa et al [1986] Ervine et al [1980], McKeogh & Elsaway [1980], Ervine & Falvey [1987], Blanchard & Cipriano [1981], and Sene [1988].

The primary objective of the experimental research was to obtain detailed local data in the two-phase flow region of a plunging liquid jet that could be used to validate multidimensional two fluid model CFD calculations. We have measured the local (turbulent) velocity of the liquid, the velocity of the gas bubbles,

Dist	Alt and/or Special
A-1	

A272970

Quality Codes

the bubble size distribution for bubbles smaller than about 1.0 mm and the void fraction of the gas phase. The combined probability density function of the bubble size and velocity has not been measured before. The probability density function for bubble diameter is needed to compute the interfacial area density, an important parameter which helps determine the mass, momentum and energy transfer characteristics of a two-phase flow. The probability density function of the bubble velocity is needed to estimate the total time that the bubbles remain submerged and therefore able to transfer mass, momentum and energy.

The spreading of a two-phase jet involves the interaction between the liquid turbulence and the bubbles. This problem can not be solved analytically. However surface depression and air entrainment can be modeled using simplifications, such as inviscid-irrotational flow theory.

Recently Lezzi and Prosperetti (1991) have proposed that the instability responsible for the air entrainment was caused by the gas viscosity. In particular, they studied the linear stability of a vertical film of a viscous gas bounded by an inviscid liquid in uniform motion on one side, and by inviscid liquid at rest on the other side. In the long wavelength asymptotic limit, the gas film behaves as a single surface and thus they obtained the classical Helmholtz result when only a surface is present. They also obtained the marginal stability boundary with the gas gap width,  $\delta$ , as the control parameter (i.e., they numerically compute for a given  $\delta$  the range of wavelength that makes the system unstable).

For the computation of jet dispersion it is important to appropriately model the turbulent intensity of the continuous phase. Single-phase turbulent jets represent an important class of free shear flows that have been studied in the past to develop and test turbulence models [Abramovich, 1963]. More recently,

turbulent jets have been evaluated numerically using computational fluid dynamic (CFD) techniques for various turbulence models. Rodi [1984] presented results using the classical  $k$ - $\epsilon$  model of Gibson & Launder [1976], and showed that  $k$ - $\epsilon$  models may not accurately predict jet spreading. Rodi [1984] proposed that the constant  $C_\mu$  in the model for turbulent viscosity was really a function of the ratio between turbulent production and dissipation. This involved the development of a new function which produced better results. Sini and Dekeyser [1987] solved the single-phase turbulent jet using Rodi's  $k$ - $\epsilon$  model [Rodi, 1984]. This model compared favorably with the experimental results of the single-phase turbulent jet as well as with other more detailed algebraic stress models. Hence it appears that in some cases turbulent nonisotropy is not important and need not be modeled.

Significantly, it has been found that single-phase turbulent jet data can be used for the assessment of turbulence models because one does not have to constitute complicated turbulent closure laws near solid (no slip) boundaries. Indeed, due to the absence of walls and the associated shear boundary conditions the turbulent jet is probably the simplest non-trivial case to analyze. Interestingly, the same conclusions can be reached for a two-phase turbulent jet.

In most of the previously mentioned research, the flow field was considered to be thin in the lateral direction and the flows were characterized by a relatively small lateral velocity when compared to the streamwise velocity. This is equivalent to considering the flow (ie, the liquid jet) to be a boundary layer. Hence, the flow is often assumed to have a negligible pressure gradient in the lateral direction, and thus the pressure in the boundary layer can be imposed by the external flow. From the mathematical point of view, this approximation changes the problem from an elliptic to parabolic one in the streamwise direction. From

the computational point of view, when using a boundary layer approximation the pressure distribution has to be prescribed. That is, the static pressure as a function of the streamwise coordinate has to be known and supplied to the computational fluid dynamic (CFD) code.

Depending on the variables of interest, approximating the jet as a boundary layer may be a reasonable approximation. However, the lateral velocity at the edge of the jet (i.e., the entrainment velocity) may be much larger than the streamwise velocity. Moreover, for a planar jet the entrainment velocity remains finite as the integration domain in the lateral direction is enlarged.

In this work we did not make the boundary layer approximation. Rather, we assumed an elliptic problem for both the gas and the liquid phases. Solving the partial differential equations as an elliptic system increases the complexity of the numerical problem but provides more detailed and accurate information on the flow field than a parabolic scheme. One of the advantages of the elliptic solution is that the streamwise pressure distribution does not have to be provided. This has two effects, first we are able to compute recirculation, and second, we are able to calculate the buoyancy-induced reversal of the bubble motion. These two important effects cannot be computed using a parabolic approach.

In parabolic single-phase jet calculations using a  $k-\epsilon$  model, Sini & Dekeyser [1987], and Hossain & Rodi [1982] found satisfactory agreement between calculations and experiments, except for a small region near the jet inlet. Their good results are due in part to the fact that they analyzed a free jet which was only weakly nonisotropic. The next level of complexity for simulating turbulent two-phase flows is the use of an Algebraic Stress Model (ASM). Several different models have been proposed in the literature. For the particular case of a planar jet, performance of the ASM is similar to the  $k-\epsilon$  model. One might expect that

the nonisotropic ASM model would produce better results than the isotropic k- $\epsilon$  model for the pressure distribution. However, when we used the ASM proposed by Gibson & Launder [1976] for the evaluation of a planar jet the computed streamwise-pressure distribution [Bergstrom, 1992] was virtually the same as when a k- $\epsilon$  model was used.

Thus, for simplicity, we have used a k- $\epsilon$  model in the computations presented in this report. We note that the turbulence present in the liquid has two components in a two-phase jet. One component, the shear-induced turbulence, is due to viscosity and it is present in both single and two-phase flows. The other component is the bubble-induced turbulence due to slip between the bubbles and the surrounding liquid, and it only occurs in two-phase flows.

## **PART-II EXPERIMENTAL RESULTS**

As shown in Figure-1, a converging nozzle oriented vertically produced an axisymmetric liquid (ie, water) jet. This jet impacted at 90° a pool of water and, when a threshold velocity was exceeded, it was observed that the plunging liquid jet caused air entrainment. In agreement with the observations of McKeogh & Ervine [1981], different two-phase jet characteristics were noted, depending on the turbulence intensity of the plunging liquid jet. For a laminar liquid jet (ie, one having a turbulence intensity less than about 0.8%) the diameter of the entrained bubbles were in the range 15-300  $\mu\text{m}$ . On the other hand, for liquid jet turbulence intensity of about 3%, the entrained bubbles had diameters in the range of 1-3 mm. Our definition of a rough and smooth jet should be considered only as an easy way to refer to one particular turbulence intensity. In particular, rough (smooth) means a turbulence intensity of about 3% (.8%). Another candidate for the distinction was the Reynolds number. However, this is not appropriate because after the contraction, with the same Reynolds number we may have different

turbulence intensity and these different turbulence intensities generate qualitatively different two-phase flows.

Figure-1 also shows a schematic of the test loop. A screw pump was used to force the water through the nozzle as well through a bypass. The pump had a speed controller which was used to make the coarse control of the liquid flow rate through the nozzle. In the bypass a valve was used for the fine control of liquid flow rate. In order to damp out any flow oscillations, an accumulator was placed on the discharge side of the pump.

The acrylic conical nozzle, shown schematically in Figure-2, consisted of an arrangement of honeycombs and screens followed by a smooth contraction. In this way the turbulence level of the liquid jet could be parametrically varied. The exit diameter of the nozzle was 5.1 mm, and this produced a liquid jet of about the same diameter. The acrylic tank which contained the water pool had dimensions,  $0.914 \times 0.916 \times 1.465 = 1.265 \text{ m}^3$ . The suction of the tank was put as far from the liquid jet impact point as possible in order to minimize the influence of this flow on the two-phase jet.

A DANTEC Fiber-Flow Laser Doppler Anemometer (LDA) system was used to nonintrusively measure the liquid and gas velocities (both the mean and fluctuations). This system consisted of submersible transmitting and receiving optics.

The receiving optics used for the smooth jet employed a Fiber Phase Doppler Anemometer (FPDA) system with 600 mm focal length lenses and a special aperture plate to maximize the bubble size range. The axial velocity of the liquid jet was used as the master signal for data collection. The collected light was transmitted through three optical fibers to a special FPDA device having three photodetectors for bubble size measurement.

The signals collected by the AT computer consisted of the:

- arrival time of the particles
- transit time of the particles
- velocity of the particles
- equivalent diameter of the particles

Two different methods were used for the measurement of void fraction in the two-phase jet: a KfK impedance probe and the particle time fraction from the FPDA. The impedance probe consists of two electrically isolated electrodes; one at the tip of the probe and another downstream electrode which was always in contact with the liquid in the pool. The liquid (ie, water) had a relatively high electrical conductivity and thus when the tip was in contact with the liquid a relatively high current flows through to a Wheatstone bridge circuit. The difference between the conductivities of the liquid and gas phases produced a different signal depending on whether there is liquid or gas present at the tip of the probe. The active element of the probe's tip was 150  $\mu\text{m}$  in diameter and it was calibrated with bubbles having diameters in the 1-3 mm range. This type of probe is a standard tool used for measuring local void fraction in air/water bubbly flows [Hewitt, 1978].

The KfK impedance probe was used to measure the void fraction in the rough jet (which had bubbles of diameter in the range 1-3 mm) because the size of bubbles produced was out of range of the FPDA (ie, the air bubbles were too large for the lens size used). In contrast, for the measurement of void fraction when a smooth liquid jet was tested, the impedance probe could not be used because the size of the bubble were the same order of magnitude as the size of the tip (ie, the air bubbles were quite small). However, the FPDA could be, and was, used to measure the size distribution of the bubbles in this case.



The FPDA was calibrated using a suspension of polystyrene particles which had a diameter of  $9.5 \mu\text{m} \pm 0.5 \mu\text{m}$ , and a rotating steel ball of diameter 0.4 mm.

The LDA/FPDA system and the KfK impedance probe were mounted on a Benjamin Systems three-dimensional traversing mechanism having a  $1 \mu\text{m}$  positioning resolution. The tip of the KfK impedance probe was positioned 0.3 mm under the measurement volume of the LDA/FPDA system for void fraction measurements when a rough jet liquid was tested.

The turbulence intensity of the liquid jet at the nozzle exit was found to be one of the most important parameters affecting jet roughness and the size of the bubbles entrained by the plunging liquid jet. An arrangement of honeycombs and screens were used to control the turbulence intensity of the flow entering the conical nozzle.

Figure-3 depicts a contour plot of the two-dimensional probability density function of the particle diameters ( $d_p$ ) and axial velocities ( $u_z$ ). Quantitatively the most probable value of peak #1 was at,  $d_p = 5 \mu\text{m}$ ,  $u_z = 4.05 \text{ m/s}$ , and the most probable value of peak #2 was at  $d_p = 125 \mu\text{m}$ ,  $u_z = 3.5 \text{ m/s}$ .

Figure-3 indicates that the velocity of the bubble was not dependent on its size. If the velocity of the bubbles had changed with size we would see the iso-count curves with their principal axes forming an angle with the horizontal. There is no such trend seen in Figure-3.

Figure-4 shows the liquid velocity histogram at the centerline of the liquid jet for a flow rate of  $w = 0.144 \text{ kg/s}$ , a distance from the nozzle to the undisturbed pool surface of  $h = 30.0 \pm 0.3 \text{ mm}$ , and a distance from the pool surface to the measurement volume of  $z = 33 \text{ mm}$ . The mean axial velocity is,  $u_1 = 4.96 \text{ m/s}$ . One of the main differences between a rough liquid jet and a smooth jet is that in

the latter case the liquid flow field is practically unaffected by the bubbles while in the former, the bubbles are much larger, thus the discrete phase increases the continuous phase's turbulence intensity. This also increases phasic momentum exchange resulting in greater dispersion of the two-phase jet and a lower velocity of the liquid velocity.

Figure-5 presents the liquid and gas velocity as a function of radial position ( $r$ ) for  $h = 17.3$  mm,  $w_l = 0.125$  kg/s and  $z = 50.0$  mm. We see that at the edge of the spreading two phase jet that the gas (bubble) velocity is negative, indicating buoyancy-driven countercurrent flow. It was also found that the two-phase jet was more dispersed than the corresponding single-phase flow case and that the turbulence intensity was higher. The turbulence enhancement is due to bubble-induced turbulence. In this case the bubble-induced turbulence accounts for about 30% of the total turbulence level.

As noted previously, when the liquid jet impacts the pool surface, air entrainment occurs around the jet's circumference. In Figure-6a the measured local void fraction is presented as a function of  $r$  for  $z = 1$  mm (i.e. with the probe 1 mm under the undisturbed liquid level). We see that the void fraction has a maximum at  $r \cong d_{jet}/2 \cong 2.5$  mm. Obviously, the air entrainment process is responsible for this effect. In the high speed video visualization of these experiments it was rare to observe bubbles at the liquid jet's centerline for  $z < 10$  mm. However, once the air was entrained, dispersion of the gas phase occurred as  $z$  was increased. Figure-6b shows how the void peaks in Figure-6a was dispersed at  $z = 18$  mm. We see that the maximum now occurs at  $r \approx 5$  mm. Moreover, we see that there is significant void fraction at  $r = 0$  (ie, the jet's centerline) because of the void dispersion process. Figure-6c shows the void fraction profile at  $z = 43$  mm. Significantly, the curve now has a maximum at the

centerline of the jet ( $r = 0$ ). Again, this is a direct result of the void dispersion process in the two-phase jet.

Figures-7a, 7b and 7c present the axial liquid velocity ( $u_l$ ) as a function of the radial distance  $r$  for three different distances ( $z$ ) from the undisturbed pool level. Figure-7a is a measurement of the liquid velocity profile at the exit of the nozzle. This flat profile is characteristic of the potential flow which exited from the nozzle.

Figures-7b and 7c show that the liquid velocity curves have a maximum at the centerline for all  $z$ . Comparing these two profiles one can easily see how the two-phase jet spreads.

Figure-8 presents the liquid and gas phasic mean velocities as a function of the lateral position ( $y$ ) for a distance between the nozzle exit and the undisturbed pool level of  $h=8.5\text{mm}$ , a liquid jet flow rate of,  $w=1.8 \text{ kg/s}$ , and a submergence of,  $z=31\text{mm}$ . We see that at the centerline the relative velocity is approximately  $0.28\text{m/s}$ . This is very close to the terminal velocity in water of a gas bubble having a 3 mm diameter. The ensemble averaged two-fluid model presented in Part-IV predicts that at a symmetry plane (where all lateral velocity gradients are zero due to symmetry) the relative velocity in the axial direction is determined by a balance between buoyancy and drag (ie, the same forces that determines the terminal velocity). Our experimental findings support this conclusion.

We see in Figure-8 that at the edge of the spreading jet the gas velocity is negative, indicating buoyancy-driven countercurrent flow. It was also found that the two-phase jet was more dispersed than the corresponding single-phase flow case. This is presumably due to the fact that the presence of the gas phase obstructs a fraction of the flow area for the liquid producing an additional acceleration of the liquid and therefore a larger momentum interchange with the

liquid pool. We also observe that the turbulence intensity was higher than in the single-phase flow due to bubble-induced pseudoturbulence.

Figure-9 shows the void fraction as a function of the lateral position ( $y$ ) for three different axial location ( $z$ ). The spreading of the dispersed phase (ie, the bubbles) can be easily seen in these plots. Figure-9 also shows the curve for  $z=1\text{mm}$  (ie, the probe 1mm under the surface) where one can see a void fraction peak at about  $y=3.5\text{ mm}$ . This peak is close to the liquid jet's edge ( $y=2.05\text{mm}$ ) and most of the air is entrained in the peak neighborhood. For  $y=0\text{mm}$  (centerplane) at  $z=1\text{mm}$  the void fraction has a minimum. This point corresponds to the liquid jet's center impacting the probe and therefore the bubble population there is very small since little lateral dispersion has occurred. Finally Figure-9 shows how the void fraction peak off the centerline is reduced as we move down into the pool and also shows significant void dispersion. Figure 10 depicts the centerline void fraction as a function of the axial position. We can also see here the local void fraction builds up.

### **PART-III: ANALYTICAL RESULTS**

The objective of this section is to evaluate the induced surface depression caused by a plunging plane liquid jet. We have assumed that both fluids are inviscid and irrotational, and that the gas region is at constant pressure. Hence the appropriate equation for this problem is Laplace's equation for the liquid and the associated interfacial jump condition. The problem may be described by two parameters, the Weber number,  $We = \frac{\frac{1}{2} \rho_l v_l^2 x_0}{\sigma}$ , and the Bond number,  $Bo = \frac{\rho_l g x_0}{\sigma}$ , where  $x_0$  is the half-width of the plunging liquid jet,  $v_l$  is the velocity of the liquid jet,  $\rho_l$  is the density of the liquid,  $g$  is the gravitational acceleration, and  $\sigma$  is the surface tension.

We have used non-singular perturbation techniques to analyze the problem. That is, we have expanded the solutions for relatively small  $We$ , and substituted these expressions into Laplace's equation and the interfacial jump condition. Equating terms of the same order in  $We$ , we obtained a recursive system of equations, which were solved numerically up to third order.

For the assumption of irrotational, inviscid flow the governing equations for the liquid field are,

$$\nabla^2 \hat{\psi} = 0 \quad (1)$$

where  $\hat{\psi}$  is the stream function. The two velocity components are then given as,

$$\hat{u} = \frac{\partial \hat{\psi}}{\partial \hat{y}} \quad (2)$$

$$\hat{v} = -\frac{\partial \hat{\psi}}{\partial \hat{x}} \quad (3)$$

where  $\hat{u}$  and  $\hat{v}$  are the velocity components along the horizontal  $\hat{x}$  and vertical  $\hat{y}$  axis, respectively. If we prescribe a value of  $\hat{\psi}$ , or its derivative normal to the surface,  $\frac{\partial \hat{\psi}}{\partial \hat{n}}$ , for every point on the boundary, we have a well-posed problem. As shown in Figure-11, the plane  $\hat{x} = 0$  is a symmetry plane. Thus the transverse lateral velocity,  $\hat{u}$ , must vanish for every  $\hat{y}$  at  $\hat{x} = 0$ . That is, from Eq. (2),

$$\hat{u}(\hat{x} = 0, \hat{y}) = \frac{\partial \hat{\psi}}{\partial \hat{y}}(\hat{x} = 0, \hat{y}) = 0 \quad (4)$$

on the centerline of the plunging liquid jet. We know that the axial velocity must be  $v_j$  at points where the jet is impacting. From Figure-11 and Eq. (3), we see that:

$$\hat{v} (0 < \hat{x} < x_0, \hat{y} = 0) = -\frac{\partial \hat{\psi}}{\partial \hat{x}} (0 < \hat{x} < x_0, \hat{y} = 0) = v_\ell \quad (5)$$

For  $\hat{x} > x_0$ , the free surface position,  $\hat{\eta}(\hat{x})$ , must be coincident with a streamline. Without loss of generality, we can make the free surface coincident with the streamline  $\hat{\psi} = 0$ . Then,

$$\hat{\psi}(\hat{x}, \hat{\eta}(\hat{x})) = 0 \quad (6)$$

We assume that the pressure in the gas region is constant and equal to zero. The liquid pressure right under the surface is related to the curvature of the surface by:

$$\frac{\sigma \frac{d^2 \hat{\eta}}{d\hat{x}^2}}{\left(1 + \left(\frac{d\hat{\eta}}{d\hat{x}}\right)^2\right)^{3/2}} = -\hat{p}_\ell(\hat{x}, \hat{\eta}(\hat{x})) \quad (7)$$

Bernoulli's equation for the liquid pressure gives

$$-\hat{p}_\ell(\hat{x}, \hat{\eta}(\hat{x})) = \frac{1}{2} \rho_\ell [\hat{u}^2(\hat{x}, \hat{\eta}(\hat{x})) + \hat{v}^2(\hat{x}, \hat{\eta}(\hat{x}))] + \rho_\ell g \hat{\eta}(\hat{x}) \quad (8)$$

We may make Eqs. (1)-(8) nondimensional, using  $x_0$  as the length scale and,  $v_\ell$  as the velocity scale, respectively. Thus we have:

$$\nabla^2 \psi = 0 \quad (9)$$

with boundary conditions,

$$\frac{\partial \psi}{\partial y}(x = 0, y) = 0 \quad (10a)$$

$$\psi(x, y \rightarrow \infty) = 0 \quad (10b)$$

$$\psi(x \rightarrow \infty, y) = 0 \quad (10c)$$

$$\frac{\partial \psi}{\partial x}(x, y=0) = 1 \quad 0 < x < 1 \quad (10d)$$

$$\psi(x, \eta(x)) = 0 \quad 1 < x \quad (10e)$$

where,

$$x = \hat{x}/x_0, \quad y = \hat{y}/x_0, \quad \eta = \hat{\eta}/x_0$$

$$u = \hat{u}/v_\ell, \quad v = \hat{v}/v_\ell \quad \text{and} \quad \psi = \frac{\hat{\psi}}{x_0 v_\ell}$$

The velocity components may now be computed from the stream function using Eqs. (2) and (3) as,

$$u(x, y) = \frac{\partial \psi}{\partial y}(x, y) \quad (11)$$

$$v(x, y) = -\frac{\partial \psi}{\partial x}(x, y) \quad (12)$$

We shall solve the problem for small  $We$  using a perturbation analysis. First, we may expand all the dependent variables in terms of  $We$  obtaining:

$$\eta(x) = \sum_{i=1}^n We^i \eta_i(x) + O(We^{n+1}) \quad (13a)$$

$$\psi(x, y) = \sum_{i=0}^n We^i \psi_i(x, y) + O(We^{n+1}) \quad (13b)$$

Substituting eqs. (13) in eqs. (10) and collecting terms of the same order in  $We$  we obtain the following boundary conditions for  $x > 1$ ,

$$\psi_0(x, 0) = 0 \quad (14a)$$

$$\psi_1(x,0) = -u_0 \eta_1 \quad (14b)$$

$$\psi_2(x,0) = -\left(u_1 \eta_1 + u_0 \eta_2 + \frac{1}{2} \frac{\partial u_0}{\partial y} \eta_1^2\right) \quad (14c)$$

$$\psi_3(x,0) = -\left(u_0 \eta_3 + u_1 \eta_2 + u_2 \eta_1 + \frac{1}{2} \frac{\partial u_1}{\partial y} \eta_1^2 + \frac{\partial u_0}{\partial y} \eta_1 \eta_2 + \frac{1}{6} \frac{\partial^2 u_0}{\partial y^2} \eta_1^3\right) \quad (14d)$$

Notice that  $\psi_i$  has homogeneous boundary conditions for  $i \geq 1$ , except for  $x \geq 1$ , where its value is given by Eqs. (14).

Substituting eqs. (13) in eq. (7) and collecting terms of the same order in  $We$  we obtain the following boundary conditions for  $x > 1$ ,

$$\frac{d^2 \eta_0}{dx^2} = Bo \eta_0 \quad (14a)$$

$$\frac{d^2 \eta_1}{dx^2} = (u_0^2 + v_0^2) + Bo \eta_1 \quad (14b)$$

$$\frac{d^2 \eta_2}{dx^2} = \left(2 u_0 \left(\frac{\partial u_0}{\partial y} \eta_1 + u_1\right) + 2 v_0 \left(\frac{\partial v_0}{\partial y} \eta_1 + v_1\right)\right) + Bo \eta_2 \quad (14c)$$

The boundary conditions for these ordinary differential equations are:

$$\eta_i(x \rightarrow \infty) = 0 \quad (15a)$$

$$\frac{d\eta_i}{dx}(x \rightarrow \infty) = 0 \quad (15b)$$

Equation (15b) results in the following ordinary differential equation,

$$\eta_1'' - Bo \eta_1 = -(u_0^2 + v_0^2) \quad (17)$$

for the interval  $1 < x < D$  with the boundary conditions,

$$\eta_1(x=D) = 0 \quad (18a)$$



$$\frac{d\eta_1}{dx}(x=D) = 0 \quad (18b)$$

Equation (17) has an integrable singular point at which  $x=1$ . We have numerically evaluated Eq. (17) using a Runge-Kutta (RK) algorithm with adaptive stepsize. Figure-12 shows  $\eta_1$  as a function of  $x$ .

Figure-13 shows the position of the interface  $\eta$  as a function of the lateral position  $x$  for values of the Weber number in the range [0.1 to 0.8]. We now analyze the behavior of the  $\eta(x)$  as we move from the rightmost position in the plot ( $x=1.1$ ) to lower values of  $x$ . For  $We = 0.1$ ,  $\eta(x)$  increases as  $x$  approaches the jet impact point  $x = 1$  without any local minimum (ie, no surface depression is present). For  $We = 0.8$ , on the other hand, as  $x$  is decreased we first have a local maximum in  $\eta$ , ( $\eta^{\max}$ ), and then a local minimum, ( $\eta^{\min}$ ). We define the depth of the surface depression,  $d$ , as:

$$d = \eta^{\max} - \eta^{\min} \quad (61)$$

Figure-14 shows the depth of the depression,  $d$ , as a function of the Weber number,  $We$ . There is no depression (ie,  $d=0$ ) up to a critical Weber number ( $We_c$ ). For  $We$  larger than the critical value, the depth of the depression increases rapidly with the  $We$ .

The depression width  $\delta$  is defined as the gas gap corresponding to a depression of  $d/2$ . Figure-15 shows  $\delta$  as a function of  $We$ . We see that for high  $We$ ,  $\delta$  levels off to a value of about 0.013.

## DISPERSION ANALYSIS

Figure-16 shows a typical plunging liquid jet. The axisymmetric liquid jet leaves the nozzle with an angle  $\theta'$ , diameter  $D_J$  and velocity  $u'_j$ . The jet velocity, diameter and impact angle are modified by gravity; the values at the pool level

being  $u_y$ ,  $D$  and  $\theta$ , respectively. The jet's inertia produces a meniscus on the surface of the pool. It is proposed that the gas entrainment is produced by an instability of the gas/liquid interfaces. The destabilizing factors are the liquid jet's velocity and gravity.

The situation is idealized as shown schematically in Figure-17. Because the induced air gap is very small compared to the diameter of the jet ( $D$ ), cartesian symmetry is assumed. Region 1 is the half width of the liquid jet ( $h_1 = D/2$ ), region-2 is the gas gap,  $h_2 \equiv \delta$ , and region-3 is the liquid pool's width ( $h_3 = \infty$ ,  $u_3 \equiv 0$ ).

The following hypotheses are made:

- (i) The fluids are inviscid, incompressible and the flow is irrotational.
- (ii) All interfaces are planar.
- (iii) The component of the gravity in the  $y$ -direction affects the stability of the flow. The effect of the gravity in the  $x$ -direction is to accelerate the flow (i.e., to make  $h_1$ ,  $h_2$  and  $h_3$  functions of  $x$ ). Because the region of interest in the  $x$ -direction is small, this effect has been neglected.
- (iv) A sinusoidal perturbation of amplitude "a" is imposed on interface A. This produces a perturbation of amplitude "b" on interface B. Both perturbations travel with celerity  $C$ .

We further assume that amplitude "a" is small enough in order to assure the validity of linear analysis. If we make a Galilean transformation with velocity  $C$ , the perturbations are standing waves and the velocity of the fluids are:  $(u_1 - C)$ ,  $(u_2 - C)$ ,  $(u_3 - C)$ , in regions 1, 2 and 3, respectively.

The appropriate conservation laws are given below:

### Mass Conservation

$$\nabla \cdot \mathbf{u} = 0 \quad (19)$$

where we have assumed that the fluids are incompressible. Since the flow is also assumed to be inviscid and irrotational, Eq. (19) reduces to:

$$\nabla^2 \phi = 0 \quad (20)$$

where,  $\underline{u} = -\nabla \phi$ , and  $\phi$  is the velocity potential.

### **Momentum Conservation**

$$\frac{\partial \underline{u}}{\partial t} + \underline{u} \cdot \nabla \underline{u} = -\frac{1}{\rho} \nabla p + \underline{g} \quad (21)$$

hence,

$$-\frac{\partial \phi}{\partial t} + \frac{1}{2} |\underline{u}|^2 + p/\rho + g_y y = \text{const.} \quad (22)$$

where,

$$u = -\frac{\partial \phi}{\partial x} = -\frac{\partial \psi}{\partial y} \quad v = -\frac{\partial \phi}{\partial y} = \frac{\partial \psi}{\partial x} \quad (23)$$

Using eqs. (22) and (23) and complex variables we obtain the following dispersion relationship:

$$\begin{aligned} & \left[ -\sigma_{12} k^2 + (u_1 - C)^2 k \rho_1 \coth(kh_1) + (u_2 - C)^2 k \rho_2 \coth(kh_2) - g_y(\rho_2 - \rho_1) \right] \\ & \times \left[ -\sigma_{23} k^2 + (u_3 - C)^2 k \rho_3 \coth(kh_3) + (u_2 - C)^2 k \rho_2 \coth(kh_2) - g_y(\rho_3 - \rho_1) \right] \\ & = (u_3 - C)^4 k^2 \rho_2^2 \operatorname{cosech}(kh_2) \end{aligned} \quad (24)$$

Equation (24) gives the wave velocity,  $C$ , for a given wave number,  $k$ . If the solution of Eq. (24) for  $C$  is a complex number with a negative imaginary part (ie,  $C_I < 0$ ) then the system is unstable, since this implies exponential growth of the form,  $\text{Exp}[-C_I kt]$ .

Equation (24) is a more general solution than the problem of interest, nevertheless it can be reduced to the plunging liquid jet case by noting:

$$\begin{aligned}
 h_1 &= D/2 & u_1 &= u & \rho_1 &= \rho_3 = \rho_l \\
 h_3 &= \infty & u_3 &= 0 & \rho_2 &= \rho_g \\
 \sigma_{12} &= \sigma_{23} = \sigma & \rho_g/\rho_l &<< 1
 \end{aligned} \tag{25}$$

Hence, the dispersion relation becomes:

$$\left[ (u - C)^2 k \coth\left(k \frac{h}{2}\right) + g \sin \theta - \frac{\sigma k^2}{\rho_l} \right] \left[ C^2 k - \frac{\sigma k^2}{\rho_l} \right] = 0 \tag{26}$$

The four solutions of Eq. (26) are:

$$C = \pm \sqrt{\frac{k}{\rho_l}} \tag{27a}$$

$$C = u \pm \sqrt{\left( \frac{\sigma k^2}{\rho_l} - g \sin \theta \right) \frac{1}{k \coth\left(\frac{kh}{2}\right)}} \tag{27b}$$

The first two solutions in Eq. (27a) are always real and therefore they do not produce interfacial instability. In contrast, one of the two roots in Eq. (27b) leads to unstable wave growth if,

$$k < \sqrt{\frac{g \rho_l \sin \theta}{\sigma}} \tag{28}$$

## GAS ENTRAINMENT RATE

We now have all the elements necessary to calculate the volumetric flow rate of air,  $Q_a$ . Figure-18 presents a schematic of the air entrainment process. Two interfacial waves of small amplitude, but wave number  $k_d$ , grow as they

move with speed  $C$ . At a certain position they touch each other entrapping a volume of air proportional to the shaded area. The shaded area,  $\Lambda$ , is given by:

$$\Lambda = 2 \int_0^{\lambda_d} \frac{\delta}{2} \left( 1 - \cos \frac{2\pi x}{\lambda} \right) dx = \delta \lambda_d$$

The corresponding volume of entrapped air is,

$$V = \pi D \Lambda = \pi \delta D \lambda_d$$

Finally, the volumetric air flow is given by:

$$Q_a = \frac{\Lambda}{\lambda_d} \pi D \lambda_d C = \pi \delta D C \quad (29)$$

Figure-19 shows the volumetric flow rate of air,  $Q_a$ , measured by McKeogh & Ervine (1981) as a function of the liquid jet velocity,  $u_l$ , for a jet diameter of,  $D = 0.0051$  m. The jet turbulence level in these experiments was 3% and the distance of the nozzle to the pool surface level was 0.03 m. We note in Figure-19 that Eq. (29) agrees well with the data. In order to further test the validity of the model we need to know the amplitude of the perturbation (i.e., the apparent roughness of the liquid jet).

## **PART-IV: NUMERICAL RESULTS**

### **THE EULERIAN LAGRANGIAN MODEL**

The momentum balance for the bubbles in component form for a two-dimensional steady-state flow can be written as:

$$\frac{D \mathbf{g}}{Dt} = \mathbf{u} \cdot \nabla \mathbf{g} \quad (30a)$$

$$\frac{D \underline{g} \cdot \underline{g}}{Dt} = \underline{g} \cdot \underline{g} \quad (30b)$$

$$\begin{aligned} \rho_g V_b \frac{D \underline{g} \cdot \underline{g}}{Dt} &= \rho_l V_b (\underline{u}_l \cdot \nabla) \underline{u}_l + C_{vm} \rho_l V_b \left[ (\underline{u}_l \cdot \nabla) \underline{u}_l - \frac{D \underline{g} \cdot \underline{g}}{Dt} \right] \\ &+ \frac{1}{2} \rho_l A_b C_D |\underline{u}_l - \underline{u}_g| (\underline{u}_l - \underline{u}_g) + (\rho_l - \rho_g) V_b \underline{g} \\ &+ C_L \rho_l V_b \underline{u}_l \times (\nabla \times \underline{u}_l) \end{aligned} \quad (30c)$$

The so-called "dirty water" Wallis drag correlation was used to compute the drag on bubbles:

$$C_D = \frac{6.3}{Re^{0.385}} \quad (31)$$

Eqs. (30) form a system of Ordinary Differential Equations (ODEs) with the position and velocity of the bubbles as dependent variables, and time as the independent variable. In this form it is a initial value problem, with the position and velocity of the bubble at time  $t=0$  the initial conditions. We have used the well known Tolmien solution for the liquid velocity field. This is a single-phase calculation of a free jet using Prandtl's mixing length theory to model the turbulence. The solid lines in Figure 20 show the trajectories of three bubbles with different initial conditions for a lift force coefficient of 0.5 (solid lines) and a lift force of 0.25(dashed lines).

Figures-20 and 21 show the emergence time and the maximum depth as a function of the jet velocity. These are two quantities of interest for mass transfer calculations. The emergence time is the time that the bubble is under water. We see in Figure-21 that the general trend is that the emergence time increases with the jet velocity. The maximum depth also increases with the jet velocity up to a  $V=2.5\text{m/s}$ . For velocities higher than 2.5 m/s the maximum depth is not very sensitive to jet velocity.

## **THE TWO-FLUID MODEL**

Different phenomenologically-based models for two-phase flows have been proposed in the past. The drawback of many of these models is that they are only applicable to particular problems. On the other hand, mechanistically-based models, commonly known as Two-Fluid Models (TFM), have been developed [Ishii, 1975; Delhay, 1968 and Drew & Lahey, 1979].

For an adiabatic plunging liquid jet entraining air bubbles, we have the following local, instantaneous conservation equations:

### **Mass**

$$\frac{\partial \rho_k}{\partial t} + \nabla \cdot (\rho_k \underline{v}_k) = 0 \quad (k = g, l) \quad (32)$$

### **Momentum**

$$\frac{\partial}{\partial t} (\rho_k \underline{v}_k) + \nabla \cdot (\rho_k \underline{v}_k \underline{v}_k) = \nabla \cdot \underline{T}_k + \rho_k \underline{g} \quad (k = g, l) \quad (33)$$

where,

$$\underline{T}_k = - p_k \underline{I} + \underline{\tau}_k \quad (34)$$

and,  $\rho_g, \rho_l, \underline{v}_g, \underline{v}_l, p_g, p_l, \underline{\tau}_g, \underline{\tau}_l$  are the phasic densities, velocities, pressures and shear stresses of the gas and liquid phases, respectively.

These local, instantaneous conservation equations may be appropriately averaged to obtain the two-fluid model. Ishii [1975] and Delhay [1968] have proposed time and spatial averages. However, the ensemble average [Drew & Lahey, 1979] seems to be the most fundamental type of averaging. An ensemble average is defined as,

$$\overline{f(\underline{x}, t)} = \int_S f(\underline{x}, t; \xi) P(\xi) d\xi \quad (35)$$

where  $f$  is the function we want to average,  $\underline{x}$  is the spatial coordinate,  $t$  is time,  $\xi$  is a parameter that determines a particular realization,  $P(\xi)$  is the probability density function, and  $S$  is the set of all realizations. We note that  $P(\xi)$  satisfies,

$$\int_S P(\xi) d\xi = 1.0 \quad (36)$$

Let us define the phase indicator function,  $\chi_k(\underline{x}, t)$ , such that it is unity if phase- $k$  is present at  $\underline{x}$  and time  $t$ , and is zero otherwise.

Thus, the volume fraction of phase- $k$ ,  $\alpha_k$ , is,

$$\alpha_k = \overline{\chi_k} \quad (37)$$

The physical interpretation of  $\alpha_k$  is as follows;  $\alpha_k(\underline{x}, t)$  is the fraction of all realizations in which phase- $k$  is present at location  $\underline{x}$  at time  $t$ .

We refer the reader to Arnold [1988] and Park [1992] for complete details on the derivation of the two-fluid model. We present here only the final results.

The ensemble-averaged continuity equation for phase- $k$  is:

### Mass

$$\frac{\partial(\alpha_k \bar{\rho}_k)}{\partial t} + \nabla \cdot (\alpha_k \bar{\rho}_k \bar{\mathbf{v}}_k) = 0 \quad (k = g \text{ or } l) \quad (38)$$

where,

$$\bar{\rho}_k = \frac{\overline{\chi_k \rho_k}}{\alpha_k} \quad (39)$$



is the ensemble-averaged phasic density.

In this work we assume that the gas and liquid densities are both constant, thus,

$$\bar{\rho}_k = \rho_k \frac{\bar{\chi}_k}{\alpha_k} = \rho_k \quad (40)$$

Next,  $\bar{v}_k$ , the ensemble-averaged phasic velocity, is given by:

$$\bar{v}_k = \frac{\overline{\chi_k \rho_k v_k}}{\alpha_k \bar{\rho}_k} \equiv \frac{\overline{\chi_k v_k}}{\alpha_k} \quad (41)$$

The ensemble-averaged momentum equation for phase-k is:

### Momentum

$$\begin{aligned} \frac{(\alpha_k \rho_k \bar{v}_k)}{\partial t} + \nabla \cdot (\alpha_k \rho_k \bar{v}_k \bar{v}_k) &= \nabla \cdot \left[ \alpha_k \left( \bar{T}_k + \bar{T}_k^{\text{Re}} \right) \right] \\ + \alpha_k \rho_k \underline{g} + \underline{M}_{ki} & \quad (k = g \text{ or } l) \end{aligned} \quad (42)$$

where,  $\bar{T}_k$ ,  $\underline{g}$ ,  $\underline{M}_{ki}$  are the averaged stress tensor, the acceleration of gravity and the total interfacial forces, respectively. They are given by:

$$\bar{T}_k = \frac{\overline{\chi_k T_k}}{\alpha_k} \quad (43)$$

$$\bar{T}_k^{\text{Re}} = -\rho_k \overline{v'_k v'_k} \quad (44)$$

where,  $v'_k$  is the fluctuation in the velocity of phase-k, and,

$$\underline{M}_{ki} = -\overline{\bar{T}_k \cdot \nabla \chi_k} \quad (45)$$

The ensemble averaged interfacial jump conditions are:

### Interfacial Jump Conditions

$$\underline{\underline{M}}_{gi} = -\underline{\underline{M}}_{li} + \nabla \cdot \left[ \alpha_g \left( \underline{\underline{\sigma}}_s + \left( \overline{p_{gi}} - \overline{p_{li}} \right) \underline{\underline{I}} \right) \right] \quad (46)$$

We note that, for monodispersed spherical bubbles, Laplace's equation yields,

$$\overline{p_{gi}} - \overline{p_{li}} = 2\sigma/\bar{R}_b \quad (47)$$

where,  $\sigma$  is the surface tension and  $\bar{R}_b$  the mean bubble radius. The bubble's surface stress tensor,  $\underline{\underline{\sigma}}_s$ , is given by [Park, 1992],

$$\underline{\underline{\sigma}}_s \stackrel{\Delta}{=} \rho_l \left[ \hat{a}_s \bar{\underline{\underline{v}}}_r \bar{\underline{\underline{v}}}_r + \hat{b}_s (\bar{\underline{\underline{v}}}_r \cdot \bar{\underline{\underline{v}}}_r) \underline{\underline{I}} \right] \quad (48)$$

where,  $\bar{\underline{\underline{v}}}_r \stackrel{\Delta}{=} \bar{\underline{\underline{v}}}_g - \bar{\underline{\underline{v}}}_l$ , is the average relative velocity, and, using inviscid flow theory, the coefficients  $\hat{a}_s$  and  $\hat{b}_s$  in Eq. (48) can be analytically computed for spherical bubbles to be:

$$\hat{a}_s = -\frac{9}{20}, \quad \hat{b}_s = \frac{3}{20} \quad (49)$$

## TURBULENCE MODELING

The total Reynolds stress tensor for the continuous liquid phase is given by superposition as,

$$\underline{\underline{\tau}}_l^{Re} = \underline{\underline{\tau}}_l^{Re(BI)} + \underline{\underline{\tau}}_l^{Re(SI)} \quad (50)$$

where, for bubbly two-phase flows the bubble-induced shear stress is given by [Arnold 1988],

$$\alpha_l \underline{\underline{\tau}}_l^{Re(BI)} = \alpha_g \rho \left[ a_l \bar{\underline{\underline{v}}}_r \bar{\underline{\underline{v}}}_r + b_l (\bar{\underline{\underline{v}}}_r \cdot \bar{\underline{\underline{v}}}_r) \underline{\underline{I}} \right] \quad (51)$$

where the coefficients  $a_l$  and  $b_l$  can be analytically computed for spherical bubbles to be,

$$a_1 = -1/20 \quad b_1 = -3/20 \quad (52)$$

We note that  $\underline{\tau}_{l(SI)}^{Re}$  is the shear-induced Reynolds stress which comes from the classical k- $\epsilon$  model [Rodi, 1984]:

$$\frac{D_l[\alpha_l k_{l(SI)}]}{Dt} = \nabla \cdot \left[ \alpha_l v_l^T \nabla k_{l(SI)} \right] + \alpha_l (P_l - \epsilon_l) \quad (53a)$$

$$\frac{D_l[\alpha_l \epsilon_l]}{Dt} = \nabla \cdot \left( \alpha_l \left[ \frac{v_l^T}{Pr_\epsilon^T} \right] \nabla \epsilon_l \right) + \alpha_l (P_\epsilon - \epsilon_\epsilon) \quad (53b)$$

where,

$$k_{l(BI)} = \frac{1}{2} \alpha_g C_{vm} |\bar{v}_r|^2 \quad (54a)$$

$$k_l = k_{l(SI)} + k_{l(BI)} \quad (54b)$$

$$v_l^t = C_\mu C_d \frac{k_{l(SI)}^2}{\epsilon_l} \quad (54c)$$

$$P_l = v_l^t (\nabla \bar{v}_l + \bar{v}_l \nabla) : \nabla \bar{v}_l \quad (54d)$$

$$P_\epsilon = C_{1e} \frac{\epsilon_l P_l}{k_{l(SI)}} \quad (54e)$$

$$\epsilon_\epsilon = C_{2e} \epsilon_l^2 / k_{l(SI)} \quad (54f)$$

$$Pr_\epsilon^T = 1.3 \quad (54g)$$

and [Rodi, 1984],  $C_\mu = 0.5478$ ,  $C_d = 0.1643$ ,  $C_{1e} = 1.44$ ,  $C_{2e} = 1.92$  are the single-phase flow k- $\epsilon$  model coefficients.

Using these results, the Reynolds stress tensor is given by:

$$\underline{\tau}_{l(SI)}^{Re} = v_l^t \left[ \nabla \bar{v}_l + \bar{v}_l \nabla \right] \quad (55)$$

After averaging, we have more unknowns than equations. Thus, we need to constitute some of the averaged quantities in terms of the state variables,  $\alpha_k$ ,  $\bar{\mathbf{y}}_k$  and  $\bar{p}_k$ . This closure process is necessary because we have lost information due to averaging and we must reintroduce the essential physics which was lost.

Cell model averaging was successfully applied to a dilute mixture of liquid and gas bubbles by Arnold [1988] and Park [1992]. We divide the flow field into "cells", each of which have only one spherical bubble inside. Using inviscid flow theory we may compute the pressure distribution around the bubbles and thus deduce the various interfacial forces. The assumptions are that both phases are inviscid, incompressible and have constant thermophysical properties, the bubbles are spherical and can be treated as a dilute dispersion of spheres, the non-uniformities in the distribution of the dispersed phase are small and the velocity gradients of both phases are small.

Using the results of Arnold [1988] and Park [1992] the resultant two-fluid phasic momentum equations are:

#### Momentum Conservation - Gas Phase

$$\begin{aligned}
 & \frac{\partial}{\partial t} (\alpha_g \rho_g \bar{\mathbf{y}}_g) + \nabla \cdot (\alpha_g \rho_g \bar{\mathbf{y}}_g \bar{\mathbf{y}}_g) = - \alpha_g \nabla \bar{p}_l \\
 & - C_{vm} \alpha_g \rho_l \left[ \left( \frac{\partial}{\partial t} + \bar{\mathbf{y}}_g \cdot \nabla \right) \bar{\mathbf{y}}_g - \left( \frac{\partial}{\partial t} + \bar{\mathbf{y}}_l \cdot \nabla \right) \bar{\mathbf{y}}_l \right] \\
 & - C_{rot} \alpha_g \rho_l \bar{\mathbf{y}}_r \times \nabla \times \bar{\mathbf{y}}_g - C_L \rho_l \alpha_g \bar{\mathbf{y}}_r \times \nabla \times \bar{\mathbf{y}}_l \\
 & - (C_1 + C_2 - 2C_p - 2b_s) \alpha_g \rho_l \bar{\mathbf{y}}_r \cdot \nabla \bar{\mathbf{y}}_r^T + (a_s - C_2) \alpha_g \rho_l \bar{\mathbf{y}}_r \cdot \nabla \bar{\mathbf{y}}_r \\
 & + (a_s - C_2) \alpha_g \rho_l (\nabla \cdot \bar{\mathbf{y}}_r) \bar{\mathbf{y}}_r + \alpha_g \rho_g \bar{\mathbf{g}} - \frac{C_D}{8} \rho_l A_i''' \bar{\mathbf{y}}_r |\bar{\mathbf{y}}_r| - C_{TD} \rho_l k_l \nabla \alpha_g \quad (56a)
 \end{aligned}$$

### Momentum Conservation - Liquid Phase

$$\begin{aligned}
 \frac{\partial}{\partial t} (\alpha_l \rho_l \bar{\mathbf{y}}_l) + \nabla \cdot (\alpha_l \rho_l \bar{\mathbf{y}}_l \bar{\mathbf{y}}_l) = & -\alpha_l \nabla \bar{p}_l + (C_p + b_s + b_l) \rho_l |\bar{\mathbf{y}}_r|^2 \nabla \alpha_g \\
 & + C_{vm} \alpha_g \rho_l \left[ \left( \frac{\partial}{\partial t} + \bar{\mathbf{v}}_g \cdot \nabla \right) \bar{\mathbf{v}}_g - \left( \frac{\partial}{\partial t} + \bar{\mathbf{v}}_l \cdot \nabla \right) \bar{\mathbf{v}}_l \right] \\
 & + C_{rot} \alpha_g \rho_l \bar{\mathbf{y}}_r \times \nabla \times \bar{\mathbf{y}}_g + C_L \rho_l \alpha_g \bar{\mathbf{y}}_r \times \nabla \times \bar{\mathbf{y}}_l + (C_2 + a_l) \alpha_g \rho_l \bar{\mathbf{y}}_r (\nabla \cdot \bar{\mathbf{y}}_r) \\
 & + (C_1 + C_2 + 2b_l) \alpha_g \rho_l \bar{\mathbf{y}}_r \cdot \nabla \bar{\mathbf{y}}_r^T + (C_2 + a_l) \alpha_g \rho_l \bar{\mathbf{y}}_r \cdot \nabla \bar{\mathbf{y}}_r \\
 & + (a_s + a_l) \rho_l (\bar{\mathbf{y}}_r \cdot \nabla \alpha_g) \bar{\mathbf{y}}_r + \alpha_l \rho_l \mathbf{g} + \frac{C_D}{8} \rho_l A_i''' \bar{\mathbf{y}}_r |\bar{\mathbf{y}}_r| + C_{TD} \rho_l k_l \nabla \alpha_g \quad (56b)
 \end{aligned}$$

where both phases were assumed to be incompressible and the following values of the closure parameters have been used [Park, 1992]:

$a_l = -1/20$	$a_s = -9/20$	$b_l = -3/20$	$b_s = 3/20$
$C_{vm} = 1/2$	$C_p = 1/4$	$C_1 = 5/4$	$C_2 = -9/20$
$C_{TD} = 0.1$	$C_L = 0.05$	$C_{rot} = 0.05$	

For numerical purposes it is important to rewrite Eq. (56a) as follows. For the air/water flows under consideration Eq. (38) can be employed to show that the left hand side of the gas phase momentum equation can be rewritten in Lagrangian form as:

$$\frac{\partial}{\partial t} (\alpha_g \rho_g \bar{\mathbf{v}}_g) + \nabla \cdot (\alpha_g \rho_g \bar{\mathbf{v}}_g \bar{\mathbf{v}}_g) = \rho_g \alpha_g \frac{D_g \bar{\mathbf{v}}_g}{Dt} \quad (57)$$

Grouping the right hand side of Eq. (57) with one part of the virtual mass force in Eq. (56a) we obtain:

$$\rho_g \alpha_g \frac{D_g \bar{v}_g}{Dt} + C_{vm} \rho_l \alpha_g \frac{D_g \bar{v}_g}{Dt} = (\rho_g + C_{vm} \rho_l) \alpha_g \frac{D_g \bar{v}_g}{Dt} \quad (6)$$

Notice that we have kept the other part of the virtual mass force associated with liquid phase acceleration in the second term on the right hand side of Eq. (56a). It has been found that writing the gas phase's acceleration as in Eq. (58) helps numerical convergence.

Equations (56) were numerically evaluated using the finite difference formulation of Patankar [1980] in the well-known PHOENICS code. The dependent variables were calculated and stored at discrete points on the grid. To prevent pressure "checker boarding" [Patankar, 1980] a staggered grid was used. The velocities are calculated at the locations. The cell surrounding point P is often called the continuity cell. The velocities,  $\bar{v}_y$  and  $\bar{v}_z$ , were computed at the cell boundaries and the pressure and void fraction,  $\bar{p}_l$  and  $\alpha_g$ , were computed at the continuity cell center (P).

According to the differencing procedure, the conservation equations were first integrated over the control volume that surrounds the node. The resulting integrals were then approximated using the nodal values and algebraic difference equations were obtained, where the discrete equations had an implicit formulation.

For the boundary conditions we used the average axial liquid and gas velocities,  $\bar{v}_{lz}$  and  $\bar{v}_{gz}$ , the liquid turbulent kinetic energy,  $\bar{v}_{lz}^2$ , and the gas void fraction  $\alpha_g$  that were actually measured at the inlet of the integration domain. Figure-23a shows the average axial liquid velocity,  $\bar{v}_{lz}$ . The open circles are the experimental values at the inlet of the domain. The solid curve is the computed

$\bar{v}_{1z}$  at the axial position  $z = 2.5$  mm (i.e., at the first velocity node), and  $y = 0.1$  m corresponds to the planar jet's centerplane.

Figure-23b shows the computed  $\bar{v}_{1z}$  at  $z = 31$  mm. The open circles are experimental points. We can see that the agreement is quite good. The spreading of the jet is well predicted and the underprediction at the center line velocity is similar to that observed in single-phase flows [Rodi, 1984]. Figure-23c shows the computed  $\bar{v}_{1z}$  at  $z = 59$  mm. The open circles are again experimental points, and the trend is similar to Figure-23b.

Figure-24a shows the gas volume fraction as a function of the lateral position. The open circles are the experimental values. The solid curve is the computed  $\alpha_g$  at the axial position  $z = 1.25$  mm (i.e. at the first gas volume fraction node). Figure-24b and 24c show the gas volume fraction as a function of the lateral position at distances from the integration domain inlet of  $z = 31$  mm and  $z = 89$  mm, respectively. We can see that the agreement is good, however, it can be noticed that the model tends to overpredict gas dispersion. For example in Figure-24c the experimental peaks are higher than the predicted ones and the experimental center plane valley is somewhat deeper than predicted.

## PART -V: SUMMARY AND CONCLUSIONS

Detailed measurements were taken of the three-dimensional void fraction and liquid velocity fields beneath a plunging liquid jet. In particular, detailed new LDA/FPDA data have been taken of the air carryunder process associated with a plunging cylindrical liquid jet. In addition, similar data (not reported herein) was taken with the planar nozzle shown in Fig-25. The size distribution of the entrained air bubbles has been measured directly with the FPDA system. It was found that for a smooth jet the entrained bubbles were very small ( $d_b \approx 120$

$\mu\text{m}$ ). For this case the slip ratio was nearly unity, and the turbulent intensity of the liquid phase was comparable to single-phase liquid jets.

The phase doppler anemometer system was found to be especially well suited for small bubble size measurements in two-phase jets. With our particular setup we could measure bubble diameters up to about 1 mm. Because of the larger bubbles present, we did not use the FPDA to measure the bubble diameters with the rough jet.

Indeed, for a turbulent (ie, rough) liquid jet the entrained bubble sizes were of the order of  $d \cong 2$  mm, and the slip ratio was close to calculated values based on the terminal rise velocity of a single bubble. Moreover, the turbulence intensity of the liquid jet had two components, one due to shear-induced turbulence and the other due to bubble-induced pseudo-turbulence. Both components of turbulence were of the same order of magnitude.

The FPDA system was found to be especially well suited for small bubble size measurements in two-phase jet flows.

A state-of-the-art two-fluid model obtained using ensemble averaging has been derived and was closed using cell average model. This approach provides equations for multiphase flows that are mechanistically-based (as opposite to empirical). The rigorous derivation of the cell average model provides exact constitutive equations for the inviscid limit. One does not expect the values of the constants from cell model averaging to be correct for very viscous flows but they provide a good framework from which to start. In particular, it is known [Wang et al, 1987] that the lift coefficient,  $C_L$ , decreases as liquid viscosity increases. In this study, a lift force coefficient of  $C_L = .05$  has been used instead of the theoretical inviscid limit value of  $C_L = .25$ . All other parameter values used in this work



corresponded to the inviscid limit values. The agreement with the experimental data was remarkable.

The  $k-\epsilon$  model seems to be adequate for this calculation, however the observed differences in phasic dispersion indicate some inadequacies in the turbulence modeling which should be considered in future studies.

This report also presents the results of an analysis based on a non-singular perturbation technique for the surface depression produced by a plunging liquid jet. The first three terms of a Taylor series expansion in the Weber number have been used to give the pool surface depression. This approximation of the surface depression gives correct values for small and moderate Weber numbers (ie,  $We < 1$ ). However, for  $We$  greater than unity, higher order terms may become important and the analysis presented herein is no longer valid. The Bond number appears as a parameter in the system of equations, thus no expansion is necessary for the Bond number. Indeed the analysis presented herein is valid for all  $Bo$ .

The results described in this report show that as the Weber number is increased, the terms that gain importance (i.e., the terms of higher order) correspond to a surface depression that is increasingly narrower in the horizontal direction. For a Weber number of the order of unity the surface tension is no longer able to keep the system stable and an Helmholtz instability leads to air entrainment [Bonetto et al, 1993]. That is, for values of the surface tension going to infinity (i.e., Weber number going to zero), the slope of the surface is very small, however, as Weber number is increased the slope also increases. For a critical value of the Weber number, the slope of the surface is such that the surface tension is not able to keep the deformed pool surface away from the plunging liquid jet and air entrainment is produced.

We have assumed in this report that the position of the interface can be written as  $\eta(x)$ , eq. 13a, that is a steady state exists where the position of the interface is a single-valued function of the lateral position. For the critical value of Weber number that corresponds to the threshold for air entrainment the interface is not single-valued. Moreover, it is likely that the air entrainment process involves transient phenomenon. Thus we believe that our analysis is not really appropriate to compute the threshold value of Weber number for air entrainment. However, we are able to describe the route to air entrainment qualitatively.

We have seen that the higher the order of the position of the interface iterate, the larger the maximum slope of the iterate. For small Weber numbers the low order iterates dominate. As Weber number is increased, the slope of the interface is increased as the higher order terms dominate. For some threshold value of Weber number,  $We_t$ , the interface has a very large slope (ie, the tangent of the interface is almost vertical). For  $We > We_t$  the inertia forces overpower the capillary forces and the interface is no longer stable.

The results presented in this report cannot predict all details of the route to the pool surface instability that produces air entrainment for two reasons. First, it is not clear that the approximation for the surface depression is valid for Weber numbers that are high enough to produce air entrainment. Second, the shape of the surface,  $\eta(x)$ , has to be a single-valued function of  $x$ , however it appears that at the point where air entrainment commences, for every  $x$  (horizontal position) there is more than one  $\eta$  (vertical position of the surface depression).

It appears that it would be useful to compute the surface position using an appropriate multidimensional Computational Fluid Dynamics (CFD) tool having

surface tracking capability. This will allow the relaxation of the restriction on Weber number.

This report presents the results of a linear stability analysis for an inviscid, irrotational and incompressible liquid jet impacting a static pool of liquid. It has been shown that a Helmholtz-Taylor instability can occur and that this instability may lead to air entrapment and carryunder. Moreover, it is shown that the thickness of the annular air gap is not a function of liquid jet velocity, however increasing the turbulence level of the liquid jet increases the wave action on the surface of the jet which leads to increased air entrainment.

It appears that it would be useful to have future experimental research on this topic focused on the effect of liquid jet viscosity, nonsymmetric situations, and nonlinear phenomena. Moreover, it should be useful to couple this type of analysis with the induced two-phase jet spreading problem below the surface of the pool. This is probably best done using appropriate interface tracking computational fluid dynamic (CFD) tools.

## BIBLIOGRAPHY

Abramovich, G.N., "The Theory of Turbulent Jets," MIT Press, 1963.

Arnold, G., "Entropy and Objectivity as Constraints Upon Constitutive Equations for Two-Phase Modeling of Two-Phase Flows," Ph.D. Thesis, Rensselaer Polytechnic Institute, 1988.

Avery, S. & Novak, P., "Oxygen Transfer at Hydraulic Structures," *Journal of Hyd. Div.*, ASCE, Vol. 104(HY11, pp. 1521-1540 (1978).

Bergstrom, D.J., "A Prediction of the Pressure Field in a Plane Turbulent Jet Using an Algebraic Stress Model," *Int. J. Numerical Methods in Fluids*, Vol. 14, pp. 907-918, 1992.

Blanchard, D. and Cipriano, R., "Bubble and Aerosol Spectra Produced by a Laboratory Breaking Wave," *J. Geophys. Res.*, Vol. 86c, p. 8085, 1981.

- Bonetto, F., Drew, D.A. and Lahey, R.T., Jr., "The Analysis of a Plunging Jet - The Air Entrainment Process," accepted for publication in *J. of Chemical Engineering Communications*, 1993.
- Bonetto, F. and Lahey, R.T., Jr., "Experimental Results of a Two-Phase Planar Jet," in preparation, 1993.
- Burgess, J.M., Molloy, N.A. and McCarthy, M.J., "A Note on the Plunging Liquid Jet Reactor," *Chem. Eng. Sci.*, Vol. 12, 442, 1972.
- Chen, C.J. and Rodi, W., "Turbulent Buoyant Jets - A Review of Experimental Data," HMT, Vol. 4, Pergamon, Oxford, 1980.
- Delhaye, J.M., "Equations Fondamentales des Ecoulement Diphasiques, Part I and II," CEA-R-3429, Centre d'Etudes Nucleaires de Grenoble, France, 1968.
- Drew, D.A. and Lahey, R.T., Jr., "Application of General Constitutive Principles to the Derivation of Multidimensional Two-Phase Flow Equations," *Int. J. Multiphase Flow*, Vol. 5, pp. 423-264, 1979.
- Detsch, R. and Sharma, R.N., "The Critical Angle for Gas Bubble Entrainment by Plunging Liquid Jets," *Chem. Eng. J.*, Vol. 44, pp. 157-166, 1990.
- Dryden, H.L. and Schuabauen, G., "The Use of Damping Screens for the Reduction of Wind Tunnel Turbulence," *JAS*, 14, pp. 221-228, April 1947.
- Durst, F., Eliasson, B., "Properties of Laser Doppler Signals and Their Exploitation for Particle Size Measurements," *Proc. LDA Symp.*, Copenhagen, 1975, pp. 115-137.
- Ervine, D.A., McKeogh, F. and Elsayay, E., "Effect of Turbulence Intensity on the Rate of Entrainment by Plunging Water Jets," *Proc. of the Institute of Civil Engineers*, Vol. 69, Part 2, pp. 425-445, 1980.
- Ervine, D.A. and Falvey, H., "Behavior of Turbulent Water Jets in the Atmosphere and in Plunging Pools," *Proc. Inst. Civil Engrs.*, Vol. 83, Part 2, pp. 295-314, 1987.
- Groth, J. and Johansson, A., "Turbulence Reduction by Screens," *J. Fluid Mechanics*, Vol. 197, pp. 139-159, 1988.
- Gibson, M.M. and Launder, B.E., "On the Calculation of Horizontal, Turbulent, Free Shear Flows Under Gravitational Influence," *J. Heat Transfer*, ASME, Vol. 98, p. 81-87, 1976.
- Hossain, M.S. and Rodi, W., "A Turbulence Model for Buoyant Flows and Its Application to Vertical Buoyant Jets," in W. Rodi (ed.), "Turbulent Jets and Plums," HMT, Vol. 6, Pergamon, New York, 1982, pp. 121-178.

- Hewitt, G.B., *Measurement of Two-Phase Parameters*, Academic Press, 1978.
- Ishii, M., "Thermo-Fluid Dynamic Theory of Two-Phase Flow," Eyrolles, 1975.
- Kerman, B.R., "A Model of Interfacial Gas Transfer for a Well-Roughened Sea," *Journal of Geophysical Research*, Vol. 89(D1), pp. 1439-1446, 1984.
- Koga, M., "Bubble Entrainment in Breaking Wind Waves," *Tellus*, Vol. 34, 481, 1982.
- Launder, B.E. and Spalding, D.B., "Lectures in Mathematical Models of Turbulence," Academic Press, New York, 1972.
- Lara, P., "Onset of Air Entrainment for a Water Jet Impinging Vertically on a Water Surface," *Chem. Eng. Sci.*, Vol. 34, 1164-1165, 1979.
- Lezzi, A.M. and Prosperetti, A., "The Stability of an Air Film in a Liquid Flow," *J. Fluid Mech.*, Vol. 226, pp. 319-347, 1991.
- Lin, T.J. and Donnelly, H.G., "Gas Bubble Entrainment by Plunging Laminar Liquid Jets," *AIChE Journal*, Vol. 12, No. 3, 563, 1966.
- Milne-Thompson, L., "Theoretical Hydrodynamics," The Macmillan Company, 1960.
- McKeogh, E.J. and Elsaway, E., "Air Retained in Pool by Plunging Water Jet," *J. of Hyd. Div.*, ASCE, 106(HY10), pp. 1577-1593, 1980.
- McKeogh, E.J. and Ervine, D.A., "Air Entrainment Rate and Diffusion Pattern of Plunging Liquid Jets," *Chem. Eng. Sci.*, Vol. 36, 1161, 1981.
- Monahan, L. and Torgersen, T., in *Air Water Mass Transfer*, edited by S. Wilhelms and J. Gulliver, American Society of Civil Engineers, 1991.
- Moral, T., "Design of Two-Dimensional Wind Tunnel Contractions," *J. Fluids Eng.*, pp. 371-378, 1977.
- Ohkawa, A., Kusabinski, D., Kawai, Y., Sakai, N. and Endoh, K., "Some Flow Characteristics of a Vertical Liquid Jet System Having Downcomers," *Chem. Eng. Sci.*, Vol. 51, pp. 2347-2361, 1986.
- Park, J.W., "Void Wave Propagation in Two-Phase Flow," Ph.D. Thesis, Rensselaer Polytechnic Institute, 1992.
- Patankar, S.V., "Numerical Heat Transfer and Fluid Flows," Hemisphere Publishing Corp., 1980.
- Prandtl, L., "Attaining a Steady Air Stream in Wind Tunnels," NACA TM 726, October 1933.

- Rae, W. and Pope, A., *Low Speed Wind Tunnel Testing*, 2nd Ed., Wiley-Interscience, 1984.
- Raithby, G.D., Galpin, P.F., Van Doormal, J.P., "Prediction of Heat and Fluid Flow in Complex Geometries Using General Orthogonal Coordinates," *Numer. Heat Transfer*, Vol. 9, pp. 125-142, 1986.
- Rodi, W., "Turbulence Models and their Application in Hydraulics," IAHR/AIRH Monograph, 1984.
- Sini, J.F., and DeKeyser, I., "Numerical Prediction of Turbulent Plane Jets and Forced Plumes by Use of the k- $\epsilon$  Model of Turbulence," *Int. J. Heat Mass Transfer*, Vol. 30, No. 9, pp. 1787-1801, 1987.
- Saffman, M., Buchhave, P. and Tanger, A., "Simultaneous Measurement of Size, Concentration and Velocity of Spherical Particles by a Laser Doppler Method," *Proceedings of the Second International Symposium on Applications of Laser Anemometry to Fluid Mechanics*, Lisbon, 1984.
- Sene, K., "Air Entrainment by Plunging Jets," *Chem. Eng. Sci.*, Vol. 43, p. 2615, 1988.
- Scheiman, J. and Brooks, J.D., "Comparison of Experimental and Theoretical Turbulence Reduction from Screens, Honeycombs, and Honeycomb-Screen Combinations," *JAS*, 18, 638-643, August 1981.
- Van De Sande, E. and Smith, J.M., "Surface Entrainment of Air by High Velocity Water Jets," *Chem. Eng. Sci.*, Vol. 28, 1161, 1973.
- Van de Sande, E. and Smith J.J., "Jet Break-up on Air Entrainment by Low Velocity Turbulent Water Jets," *Chem. Eng. Sci.*, Vol. 31, 218, 1976.
- Wang, S.K., Lee, S-J., Lahey, R.T., Jr. and Jones, O.C., Jr., "3-D Turbulence Structure and Phase Distribution Measurements in Bubbly Two-Phase Flows," *Int. J. Multiphase Flow*, Vol. 13, No. 3, pp. 327-343, 1987.

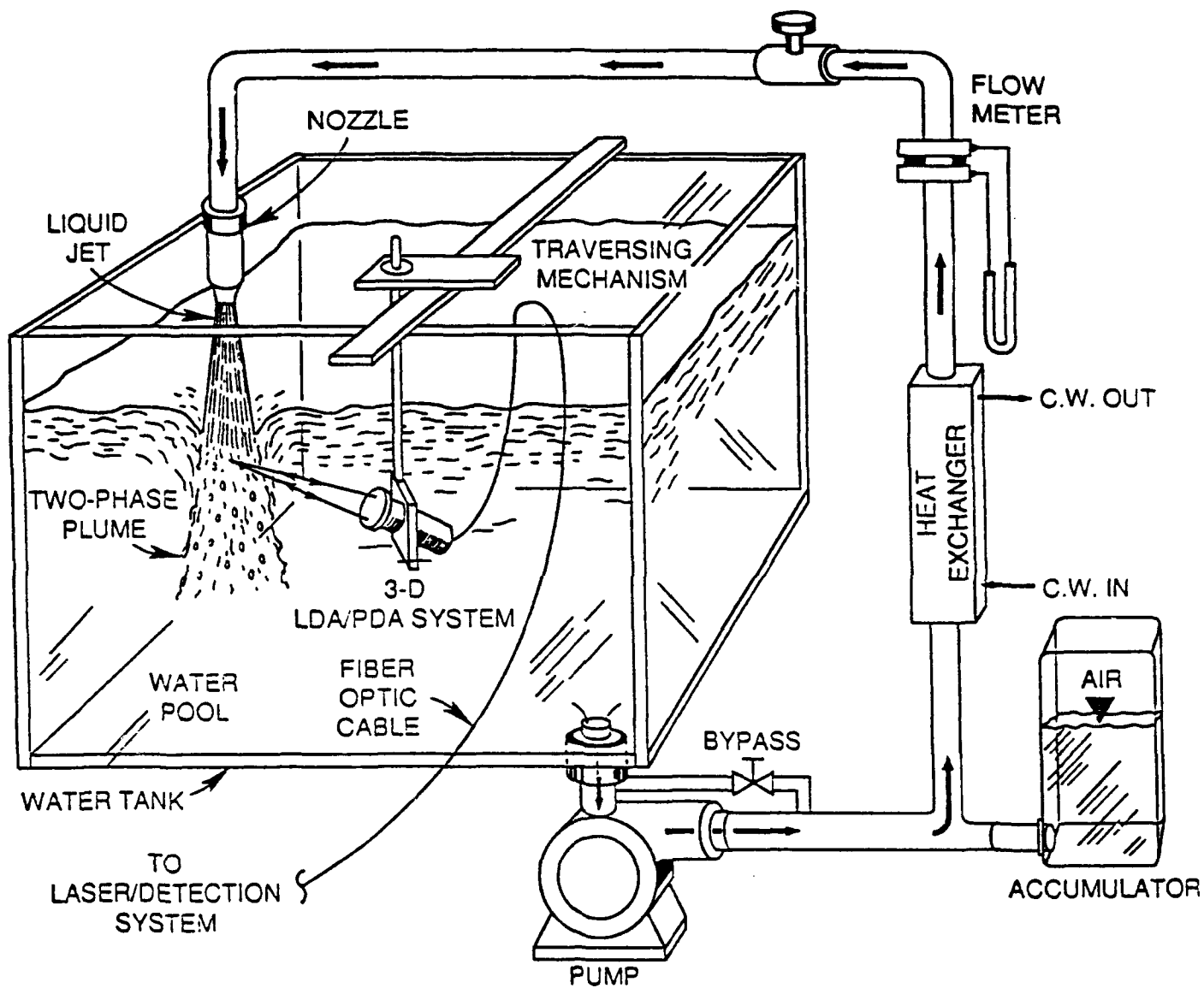


**Figure 1 Schematic of the Experimental Apparatus**

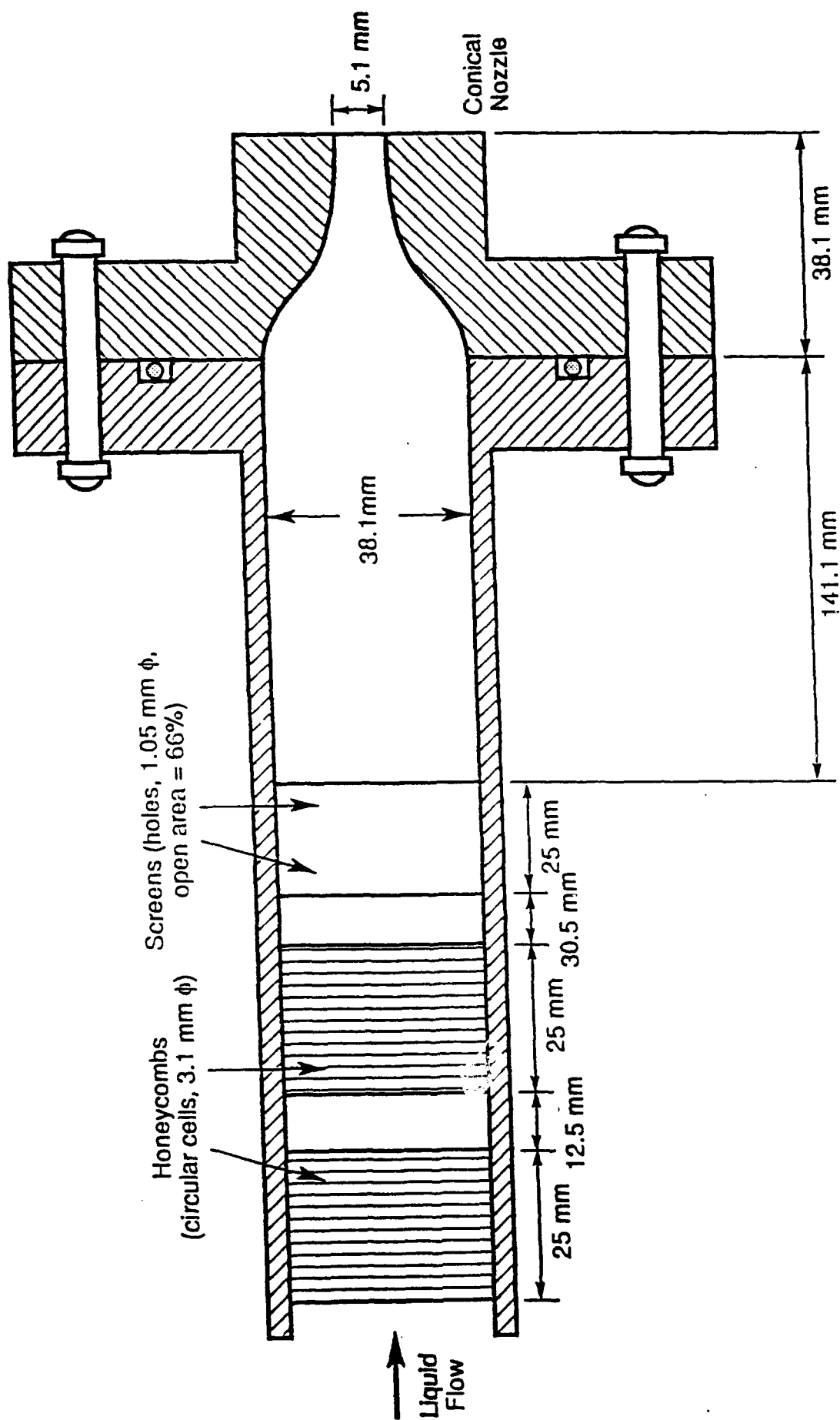


Figure 2 Schematic of the Conical Nozzle



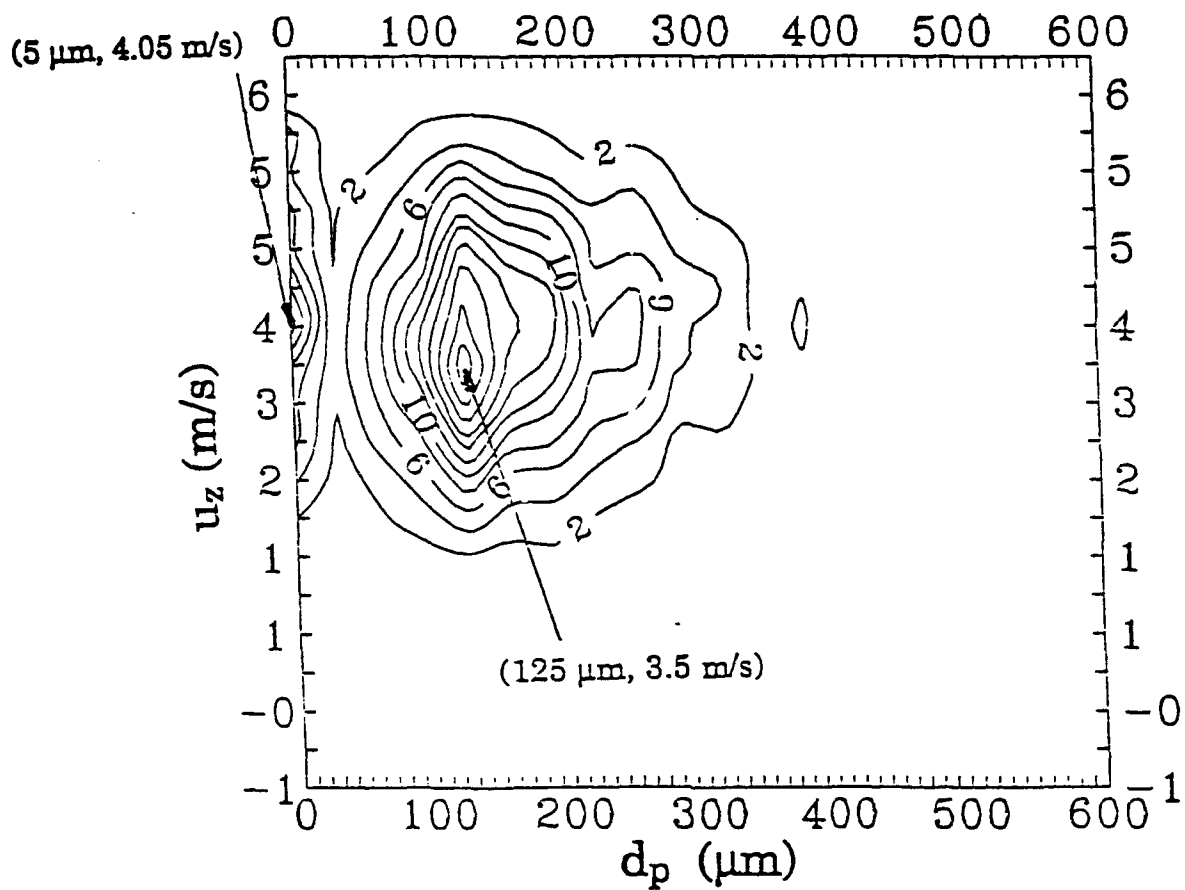


Figure 3 Contour Plot of the Two-Dimensional Probability Density Function - Smooth Jet ( $z = 35.1 \text{ mm}$ ;  $w_t = 0.143 \text{ kg/s}$ ;  $h = 9.0 \text{ mm}$ ;  $r = 0$ )

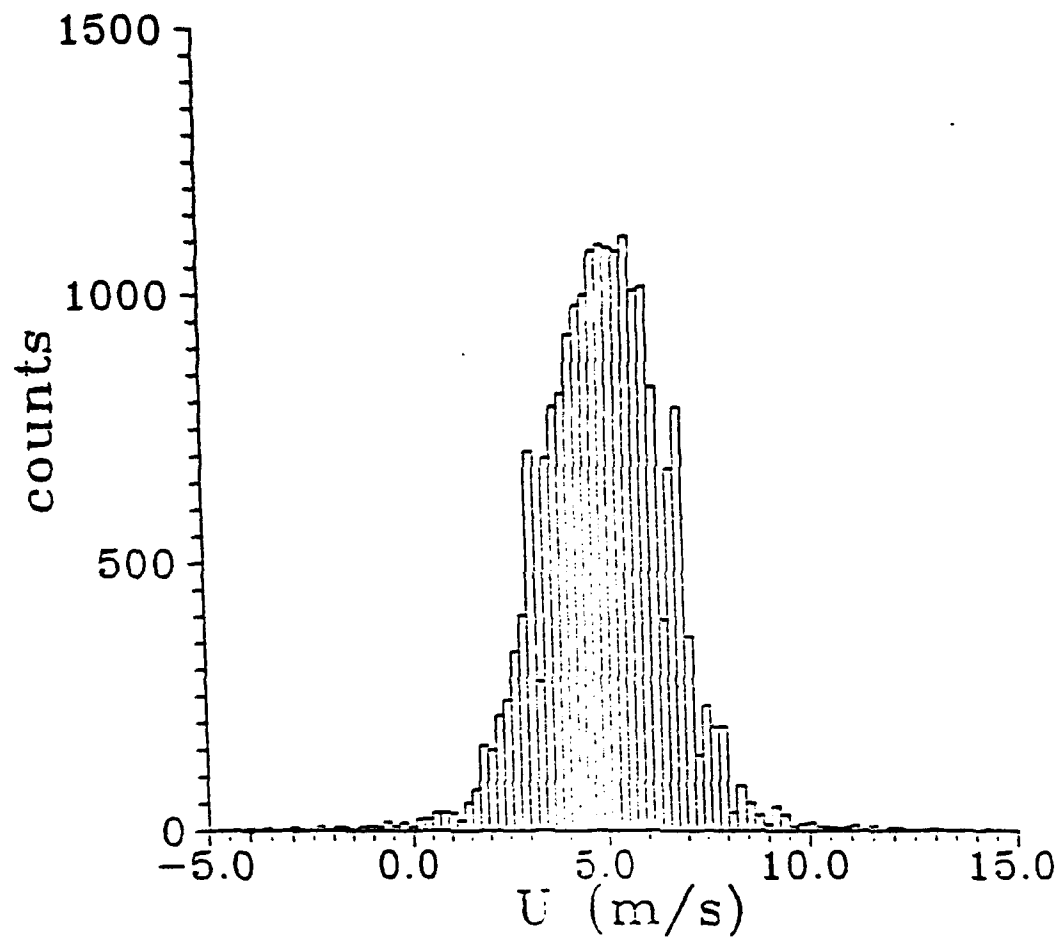
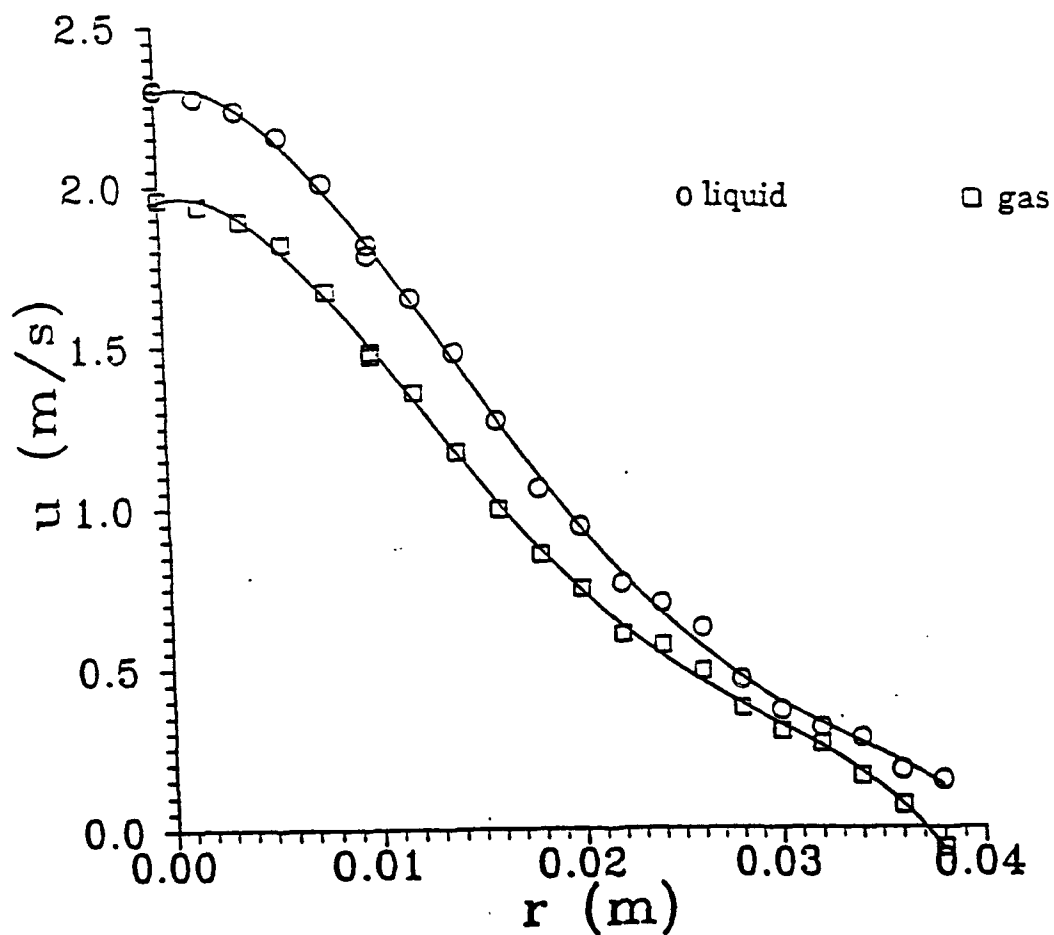


Figure 4 Liquid Velocity Histogram - Rough Jet  
( $z = 33$  mm;  $w_l = 0.144$  kg/s;  $h = 29.9$  mm;  $r = 0$ )



**Figure 5** Liquid and Gas Mean Velocities as a Function of the Radial Distance  
 - Rough Jet ( $z = 50.0 \text{ mm}$ ;  $w_l = 0.125 \text{ kg/s}$ ;  $h = 17.3 \text{ mm}$ )

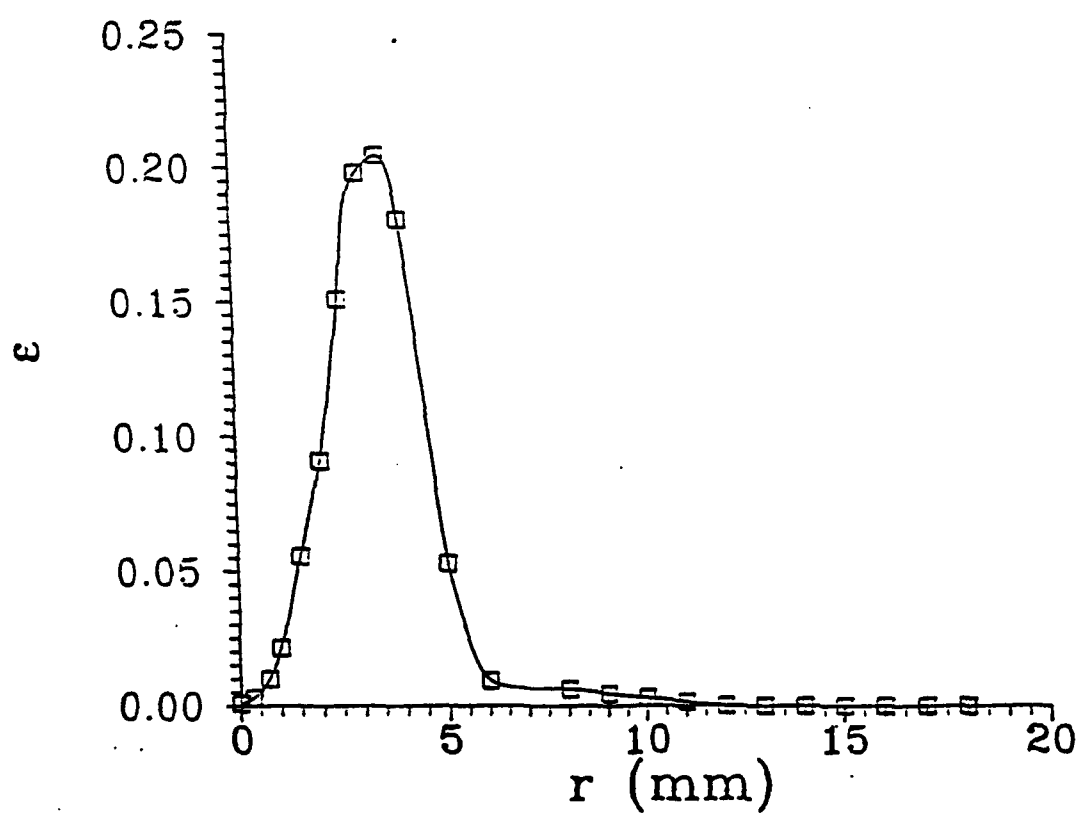


Figure 6a Void Fraction as a Function of Distance from the Center-Line -  
Rough Jet ( $w_t = 0.181$  kg/s;  $h = 30$  mm;  $z = 1$  mm)

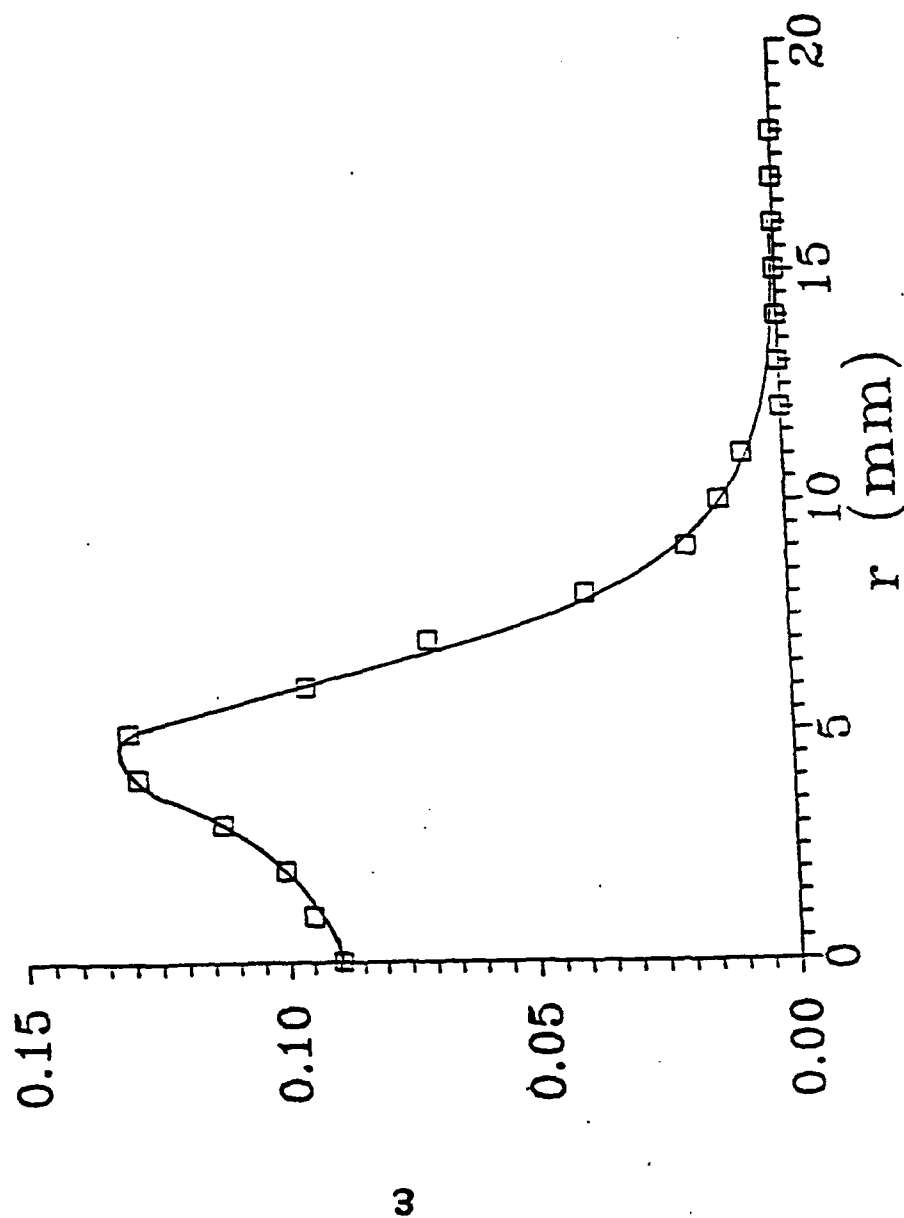


Figure 6b Void Fraction as a Function of Distance from the Center-Line -  
 Rough Jet ( $w_t = 0.181$  kg/s;  $h = 30$  mm;  $z = 18$  mm)

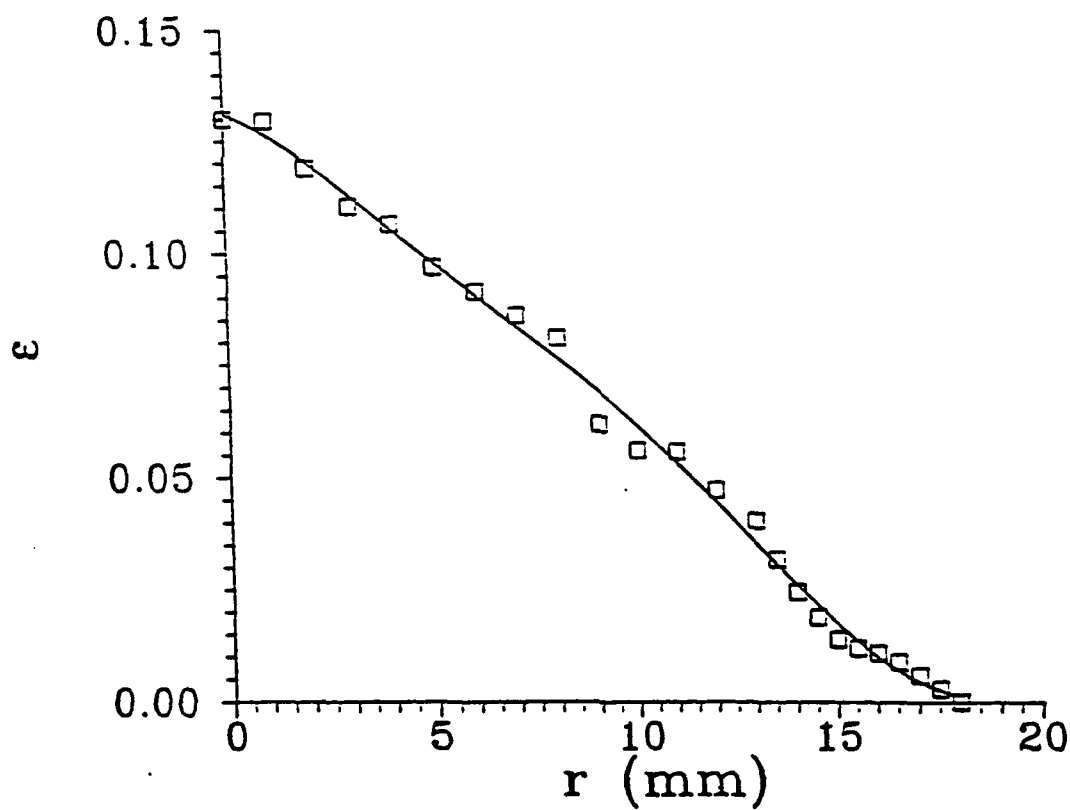


Figure 6c Void Fraction as a Function of Distance from the Center-Line -  
Rough Jet ( $w_t = 0.181$  kg/s;  $h = 30$  mm;  $z = 43$  mm)

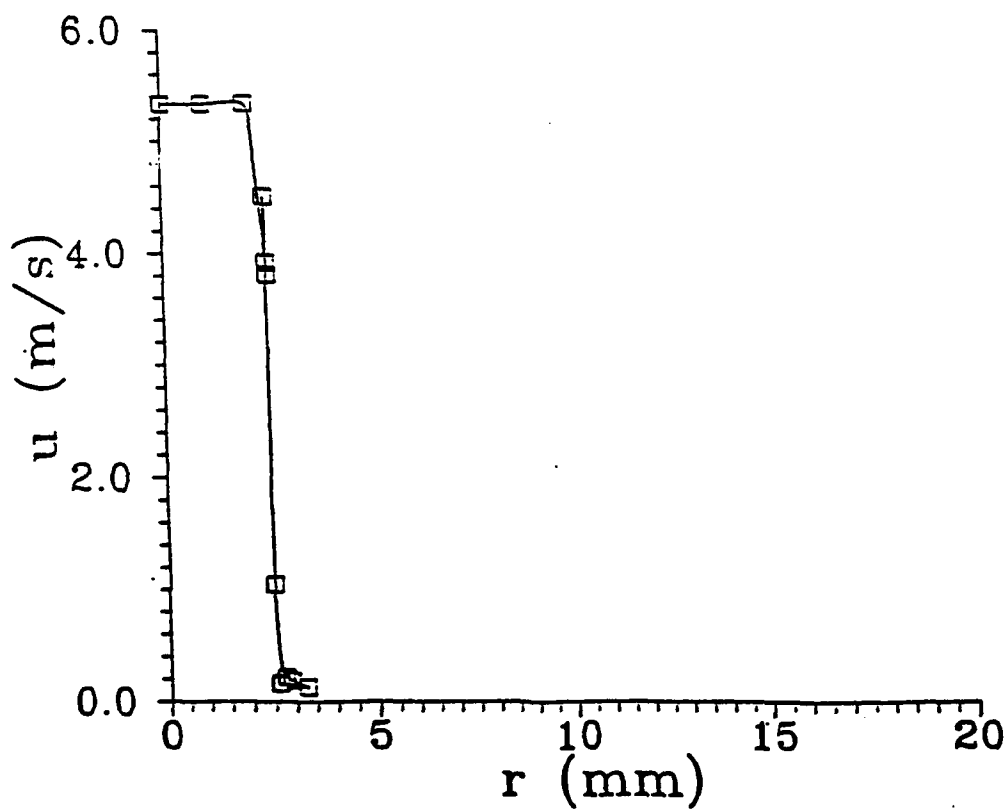


Figure 7a Liquid Velocity as a Function of Distance from the Center-Line -  
Rough Jet ( $w_l = 0.107$  kg/s;  $h = -30$  mm;  $z = 0.1$  mm)

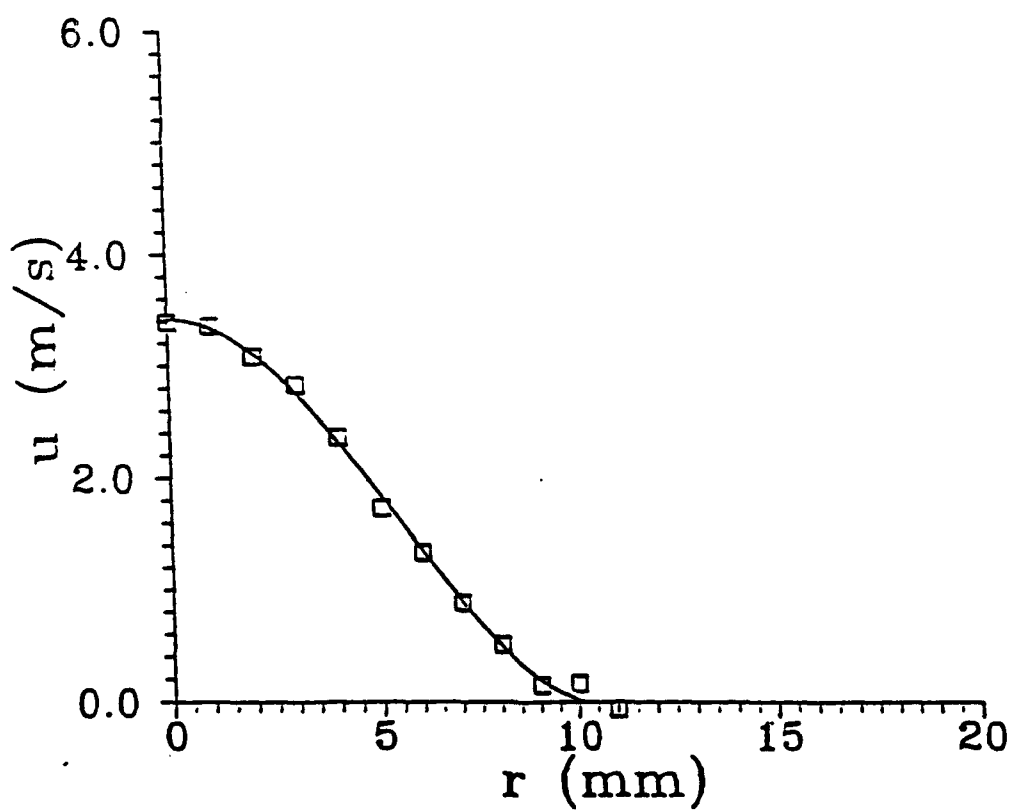


Figure 7b Liquid Velocity as a Function of Distance from the Center-Line -  
Rough Jet ( $w_t = 0.107$  kg/s;  $h = 10$  mm;  $z = 18$  mm)



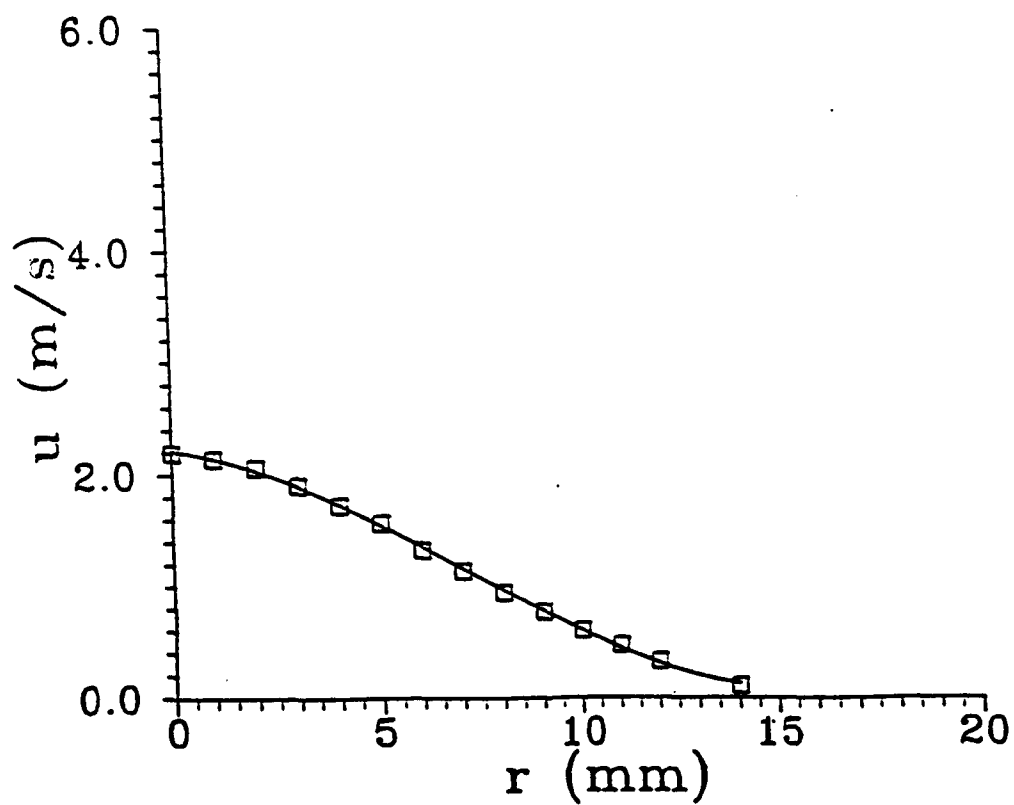


Figure 7c Liquid Velocity as a Function of Distance from the Center-Line -  
Rough Jet ( $w_t = 0.107 \text{ kg/s}$ ;  $h = 10 \text{ mm}$ ;  $z = 43 \text{ mm}$ )

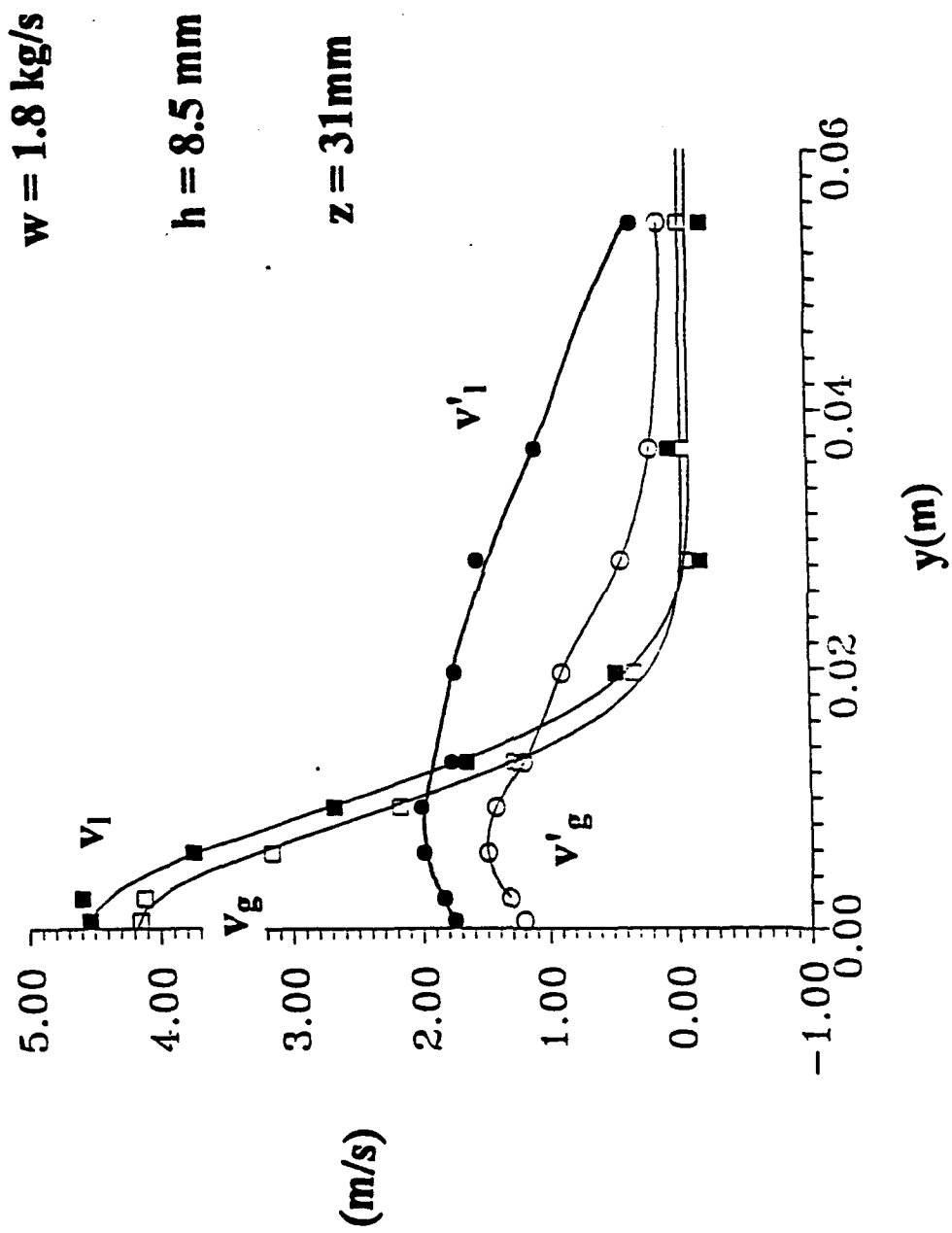


Figure-8: Mean and rms axial velocities for the gas and liquid phases.

$w = 1.8 \text{ kg/s}$

$h = 8.5 \text{ mm}$

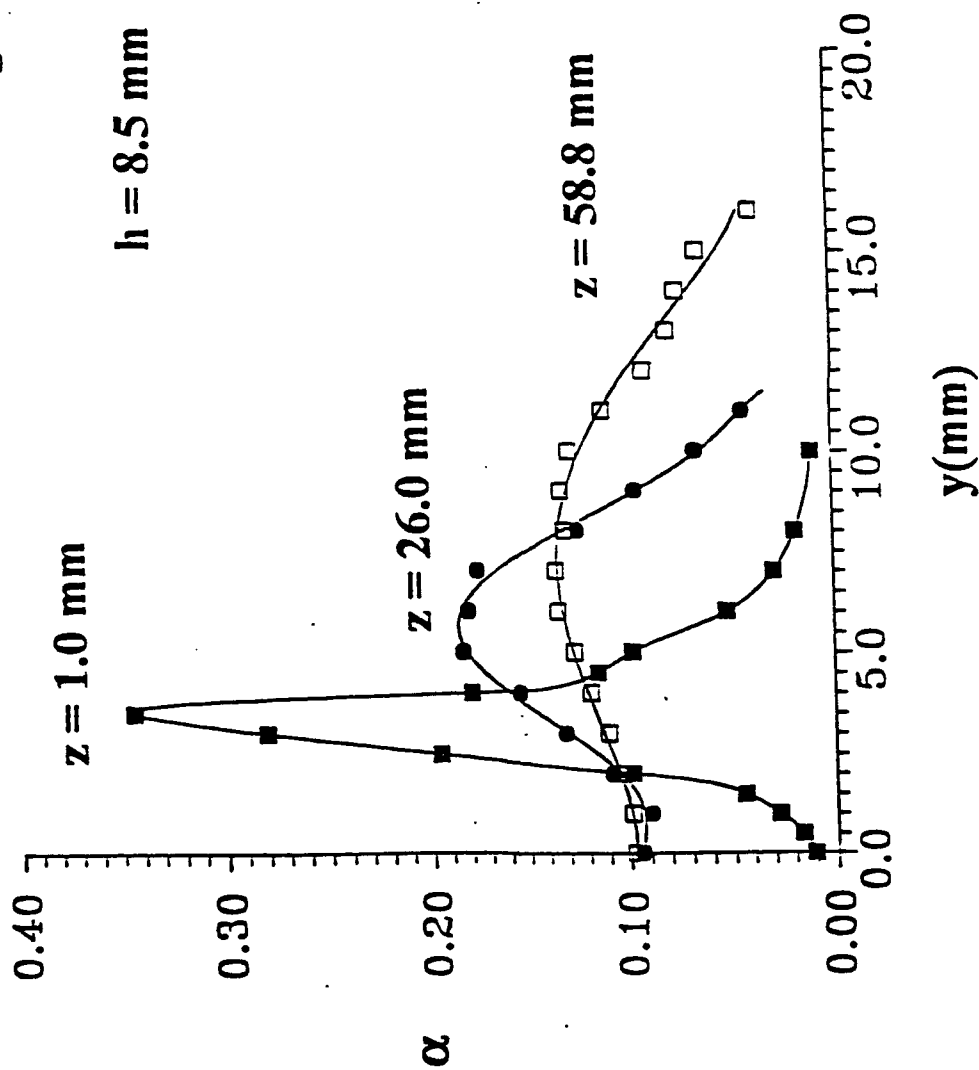
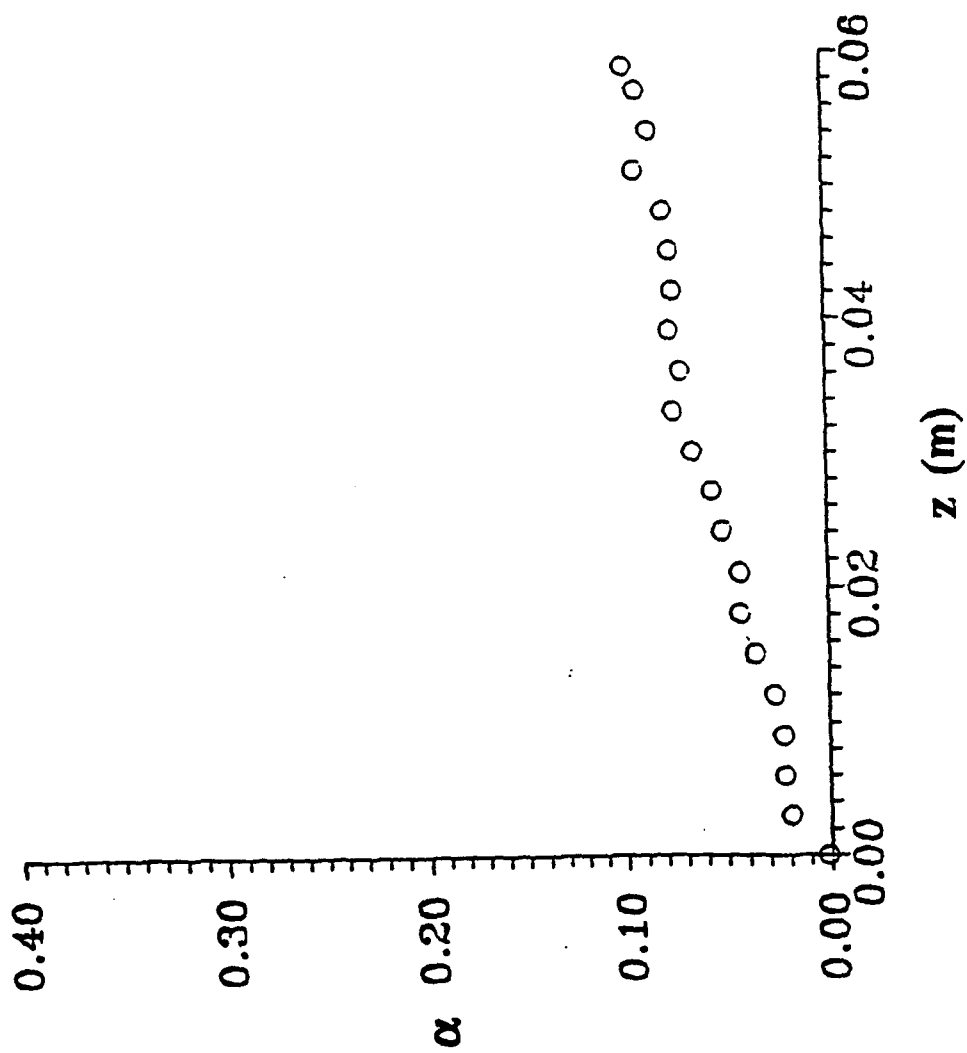


Figure-9: Void fraction as a function of the lateral position for different axial positions.



$w = 1.8 \text{ kg/s}$

$h = 8.5 \text{ mm}$

$y = 0 \text{ mm}$

**Figure-10 Centerline void fraction as a function of the axial position.**

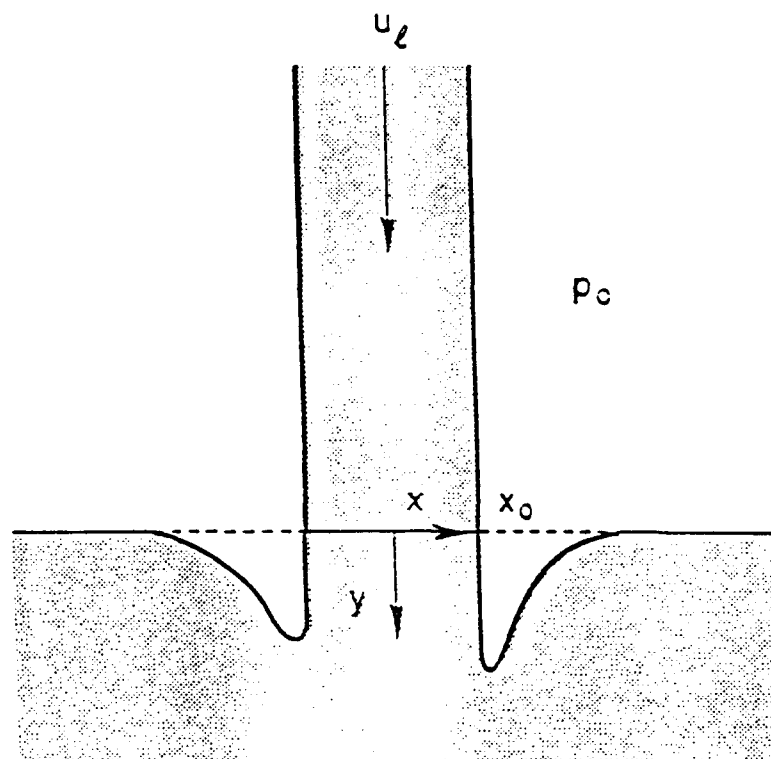


Figure 11 Illustration of the surface depression produced by a plunging liquid jet.

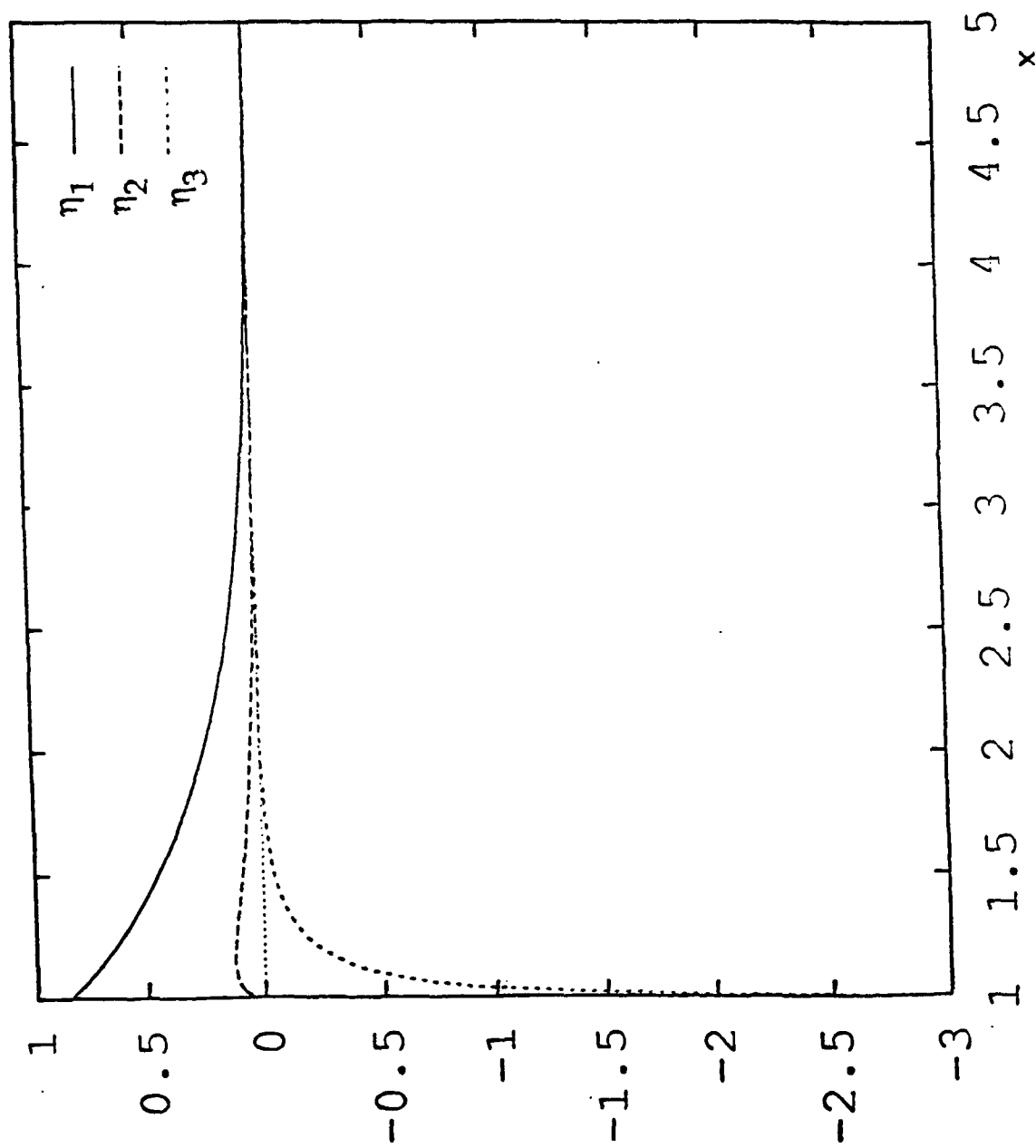


Figure 12 Iterates of the surface position,  $\eta_i(x)$ , corresponding to  $Bo=0$

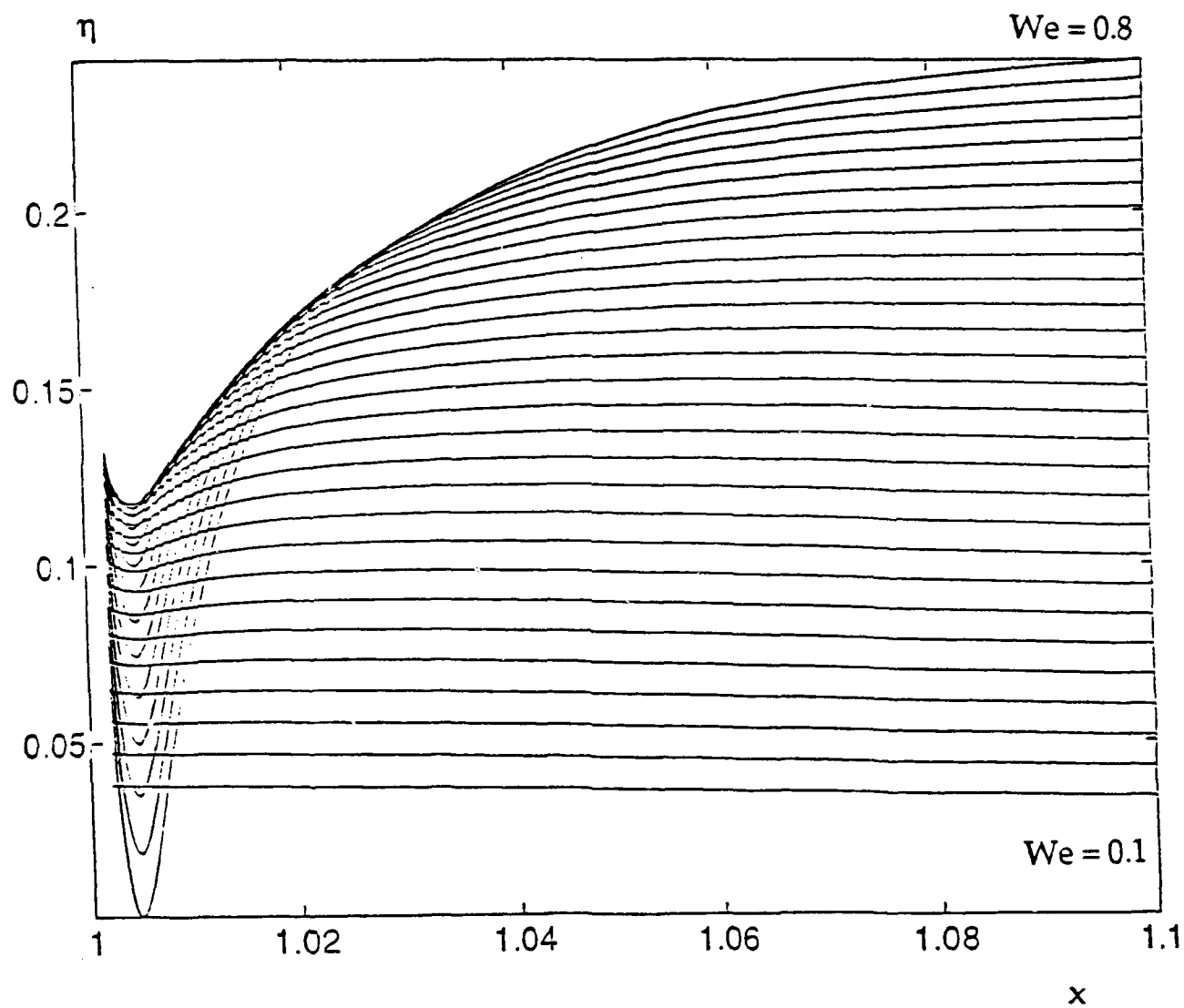


Figure 13 Shape of the interface for different Weber numbers( $Bo=0$ )

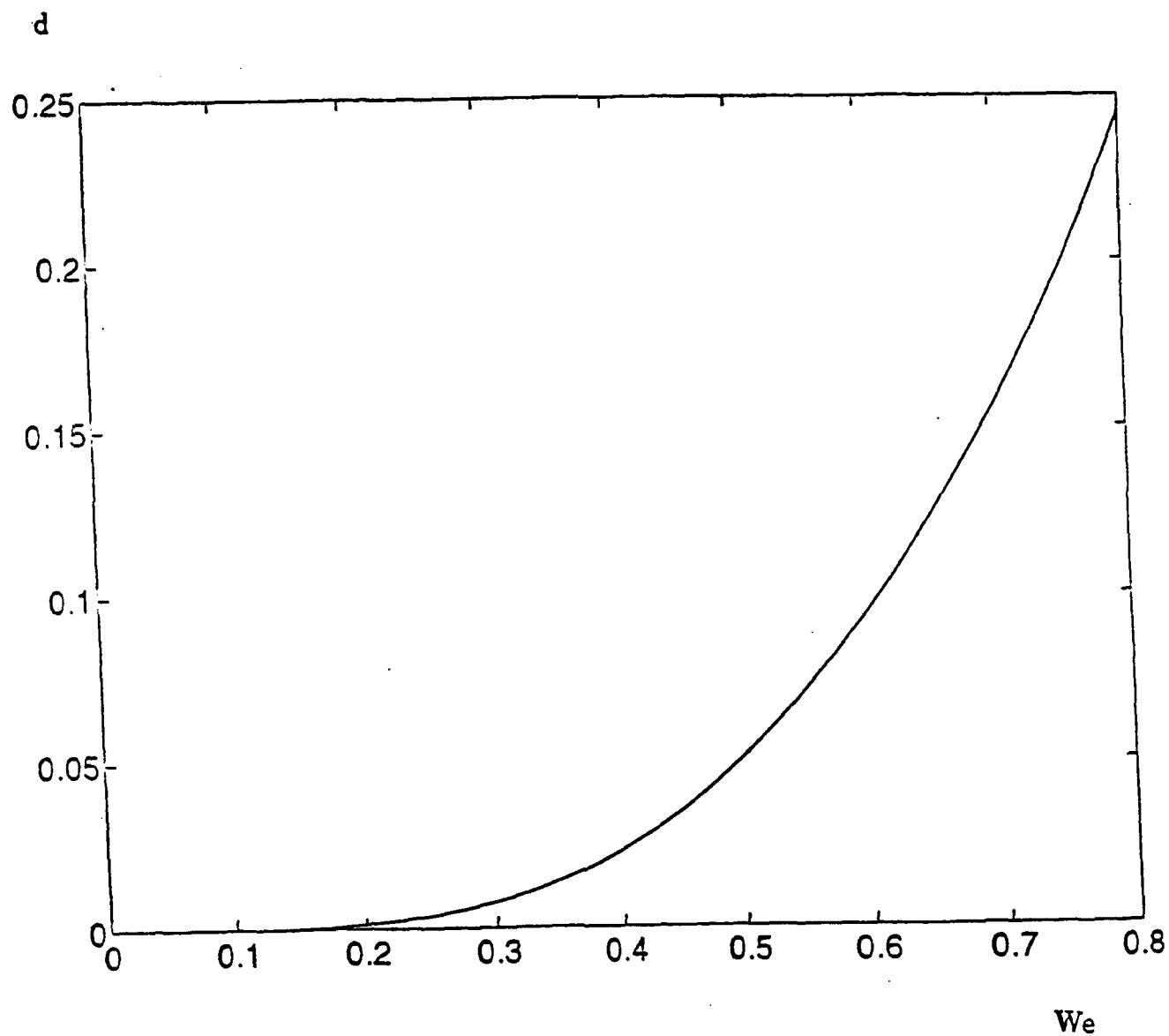


Figure 14 Gas gap depth  $d$  as a function of the Weber number ( $Bo=0$ ).



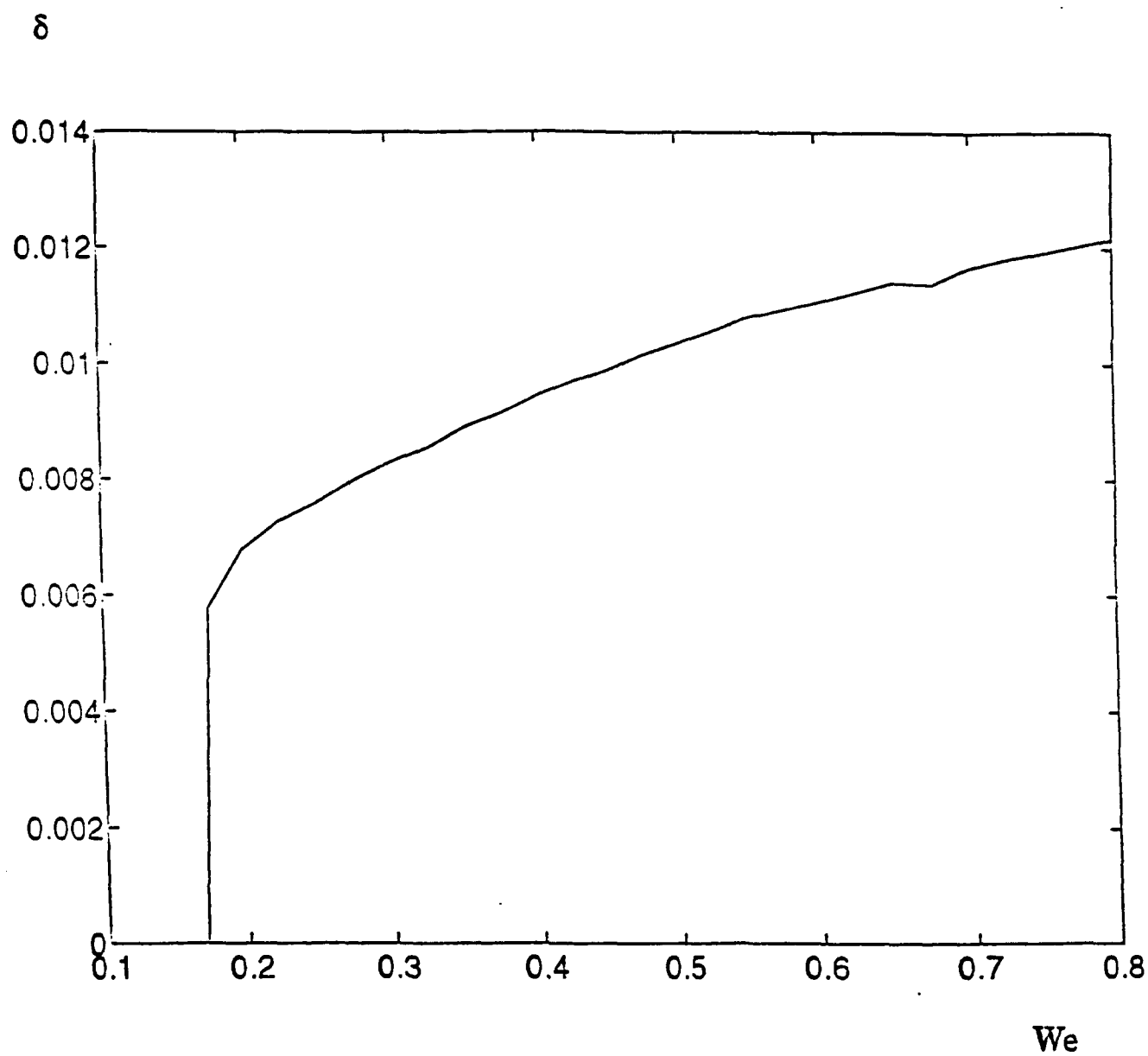


Figure 15 Gas gap width  $\delta$  as a function of the Weber number ( $Bo=0$ )

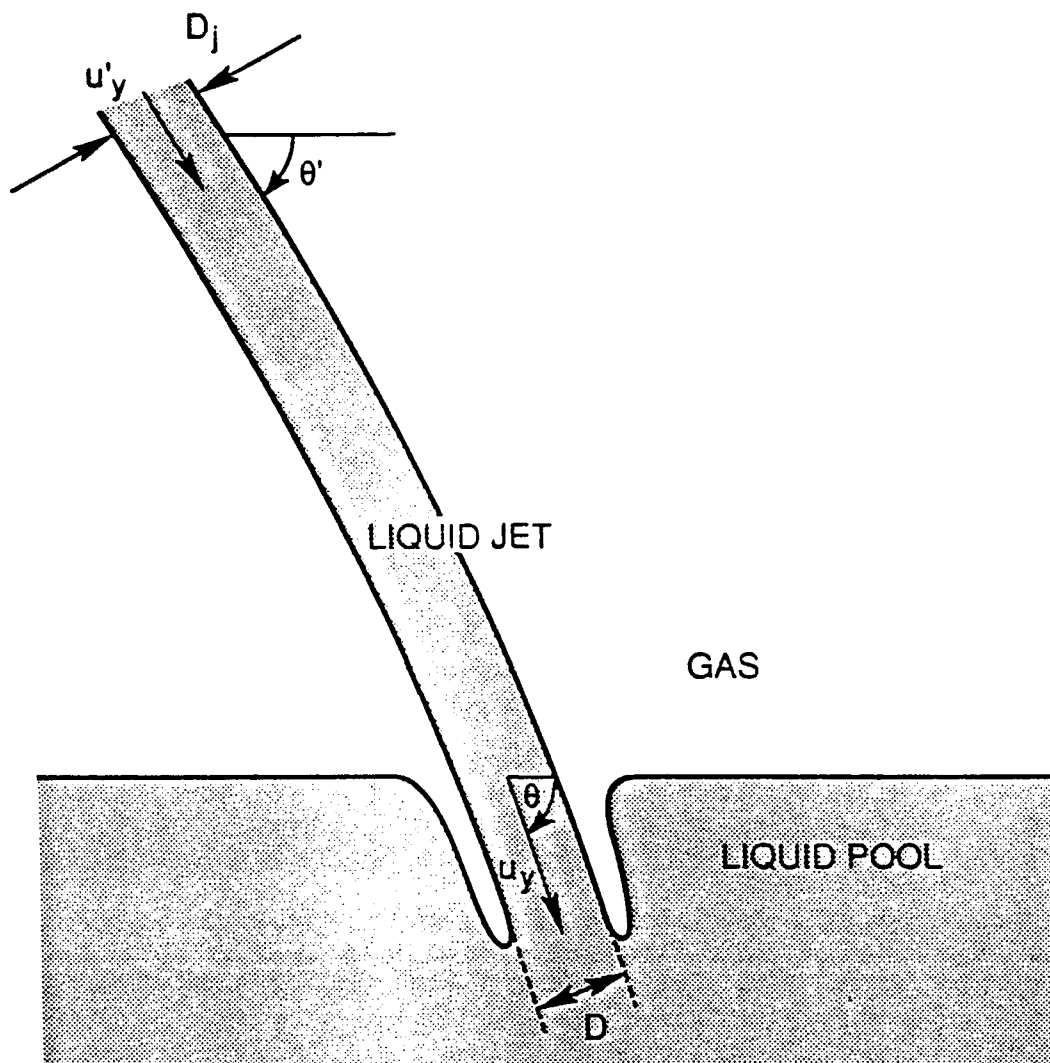


Fig. 16 The Plunging Liquid Jet.

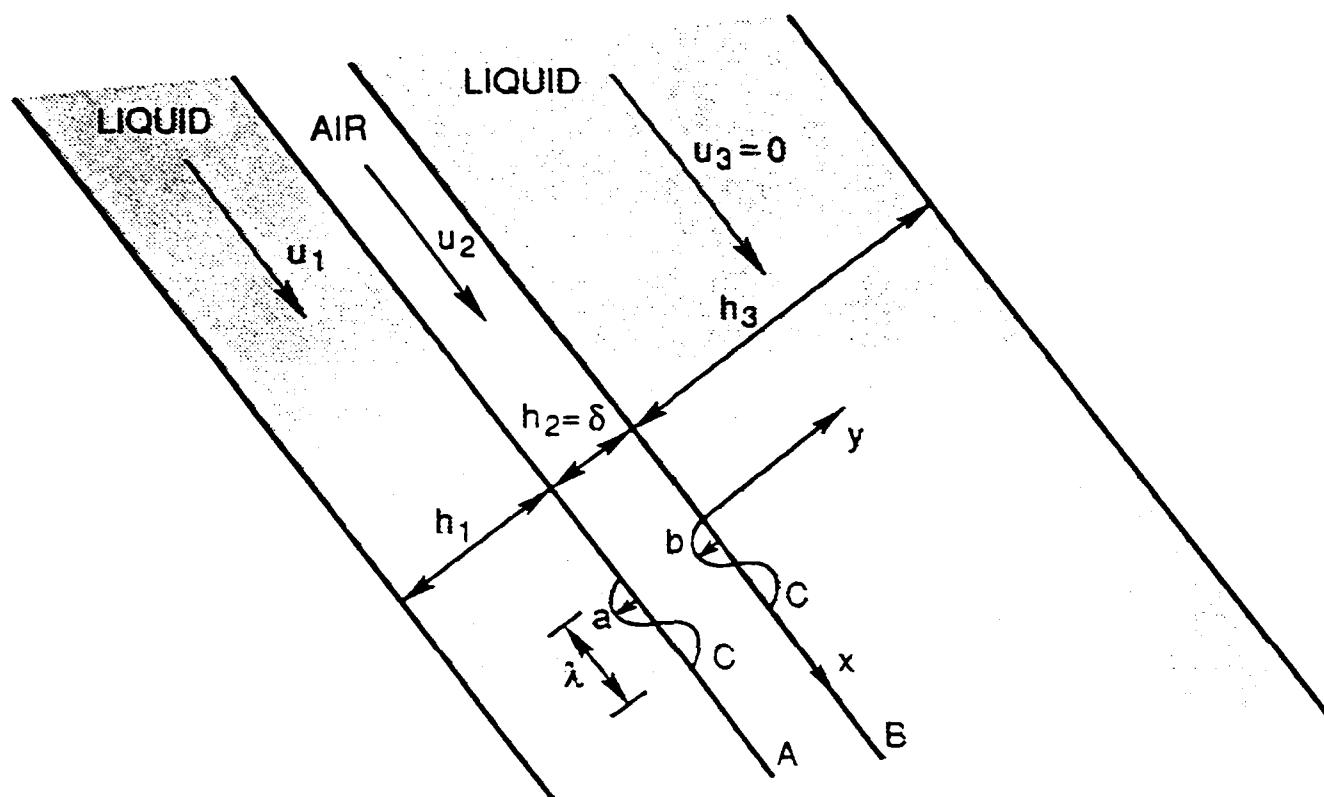


Fig. 17 Schematic Diagram of the Plunging Liquid Jet Just Below the Pool Surface.

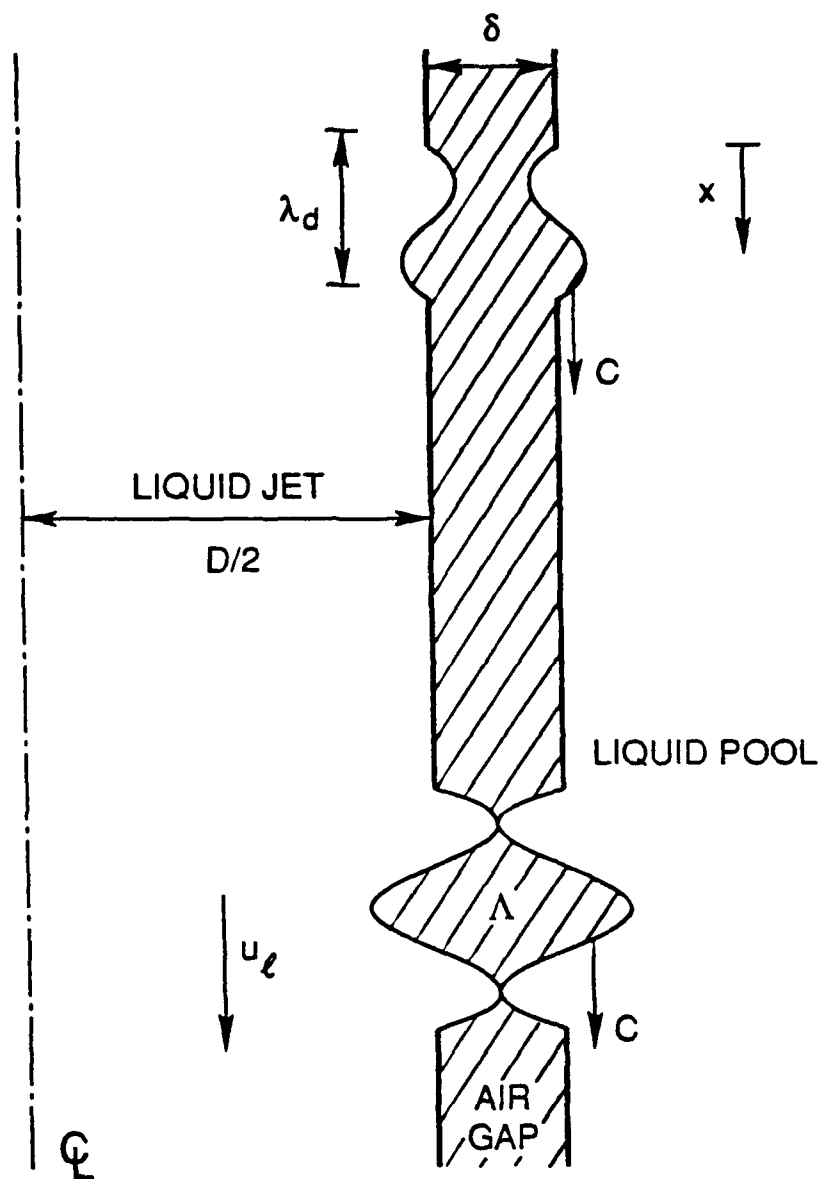


Fig. 18 Mechanism Responsible for Air Entrainment.

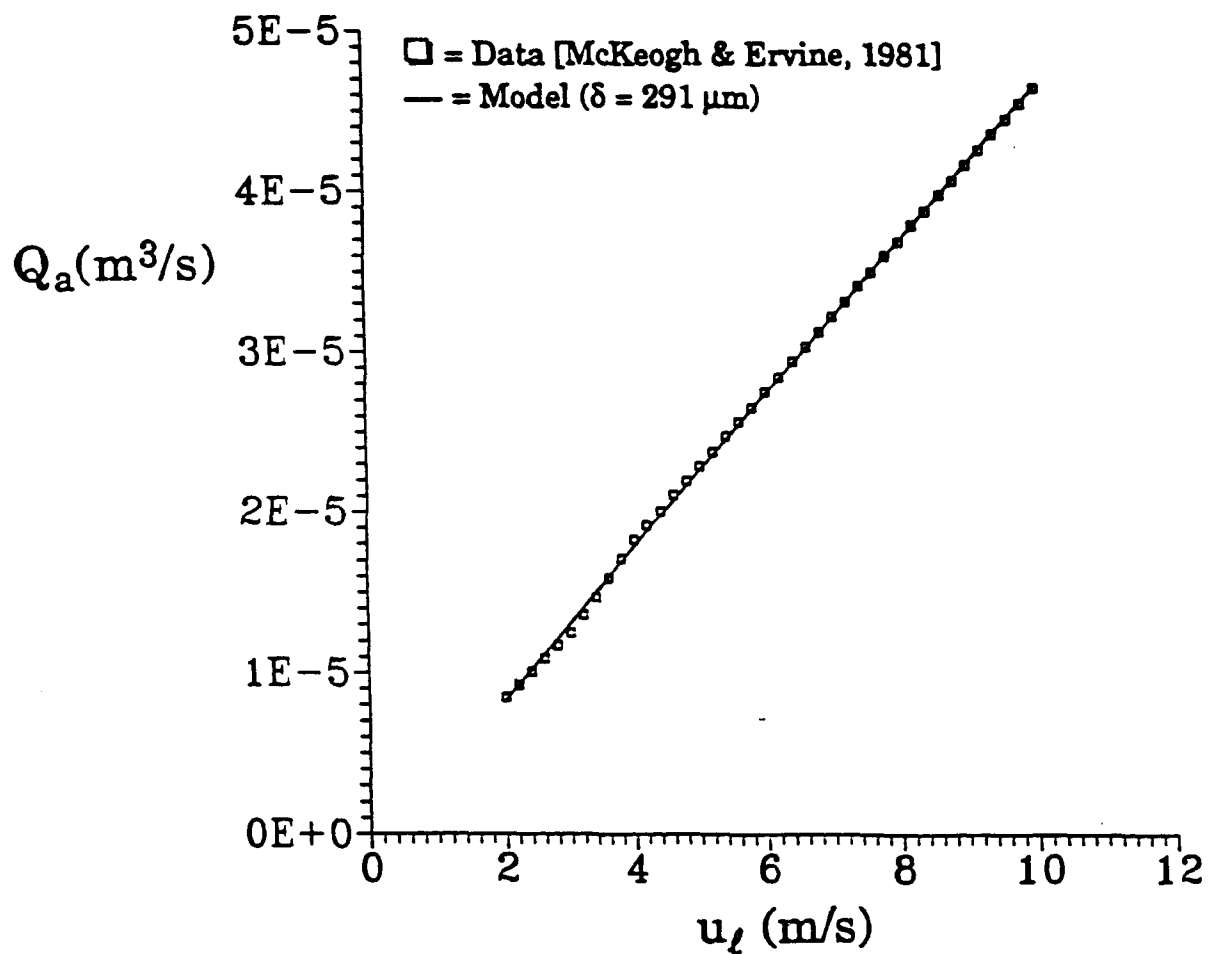
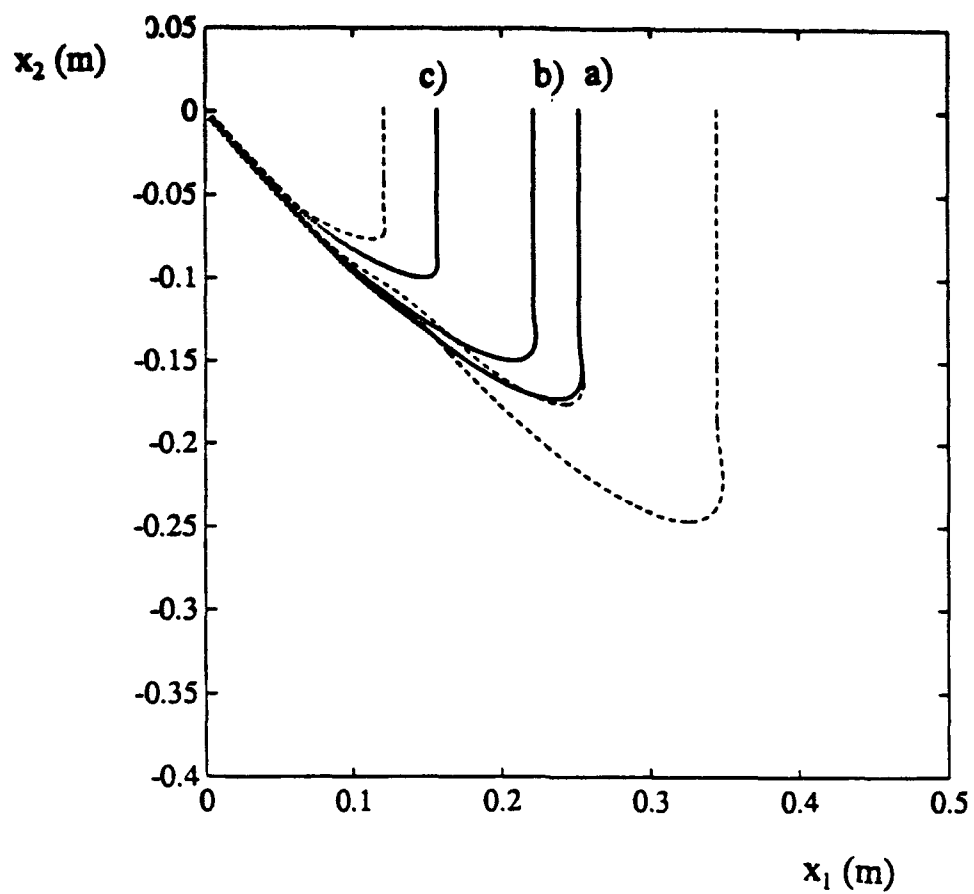


Fig. 19 Air Volumetric Flow Rate As A Function Of Jet Velocity



$C_L = 0.25$   
 $C_{VM} = 0.5$   
 $\theta = 45$   
 $V = 5 \text{ m/s}$   
 $R_b = 0.002 \text{ m}$

Figure 20 Bubble trajectories for  $C_L = 0.25$  and different initial positions

a)  $y(t=0) = -h/2$

b)  $y(t=0) = 0$

c)  $y(t=0) = +h/2$

The dashed lines are the base solutions

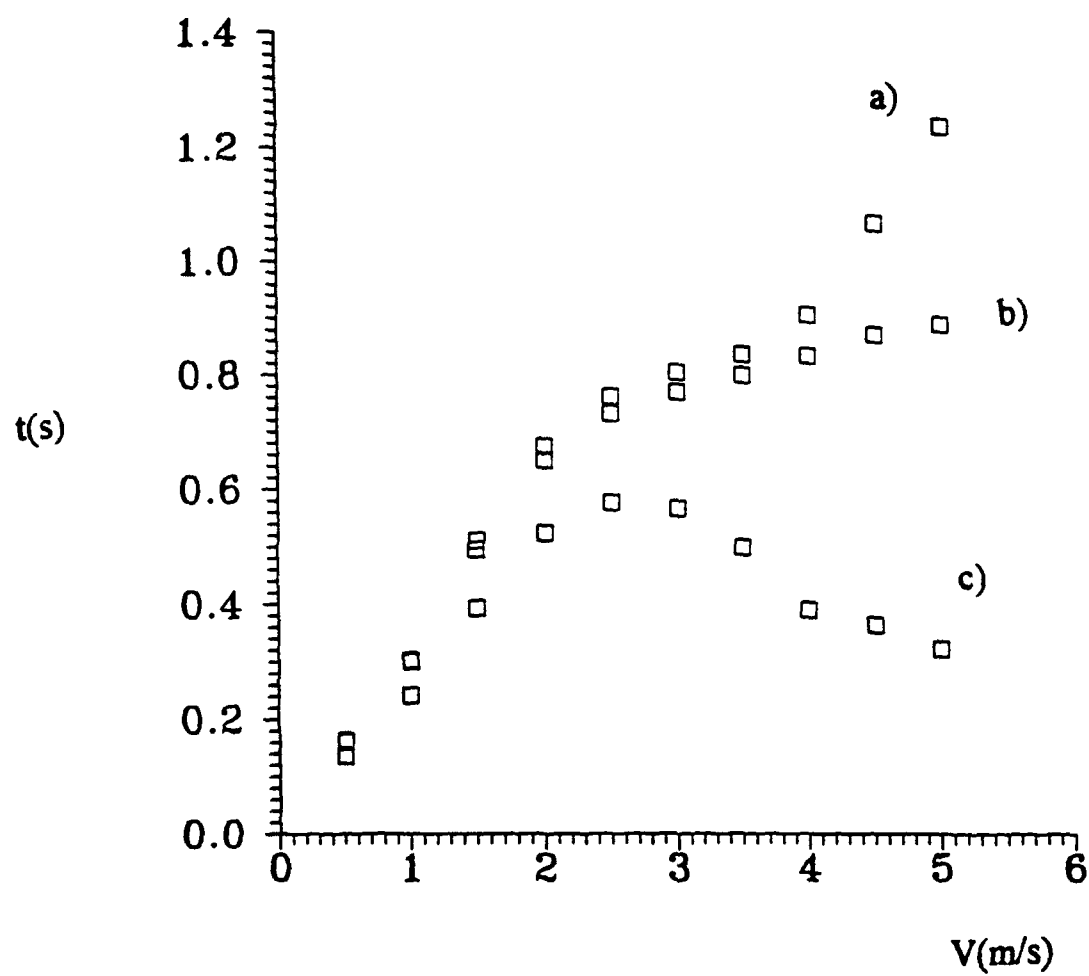


Figure 21 Emergence time  $t$  as a function of the jet velocity for different initial positions:

- a)  $y(t=0)=-h/2$
- b)  $y(t=0)=0$
- c)  $y(t=0)=+h/2$

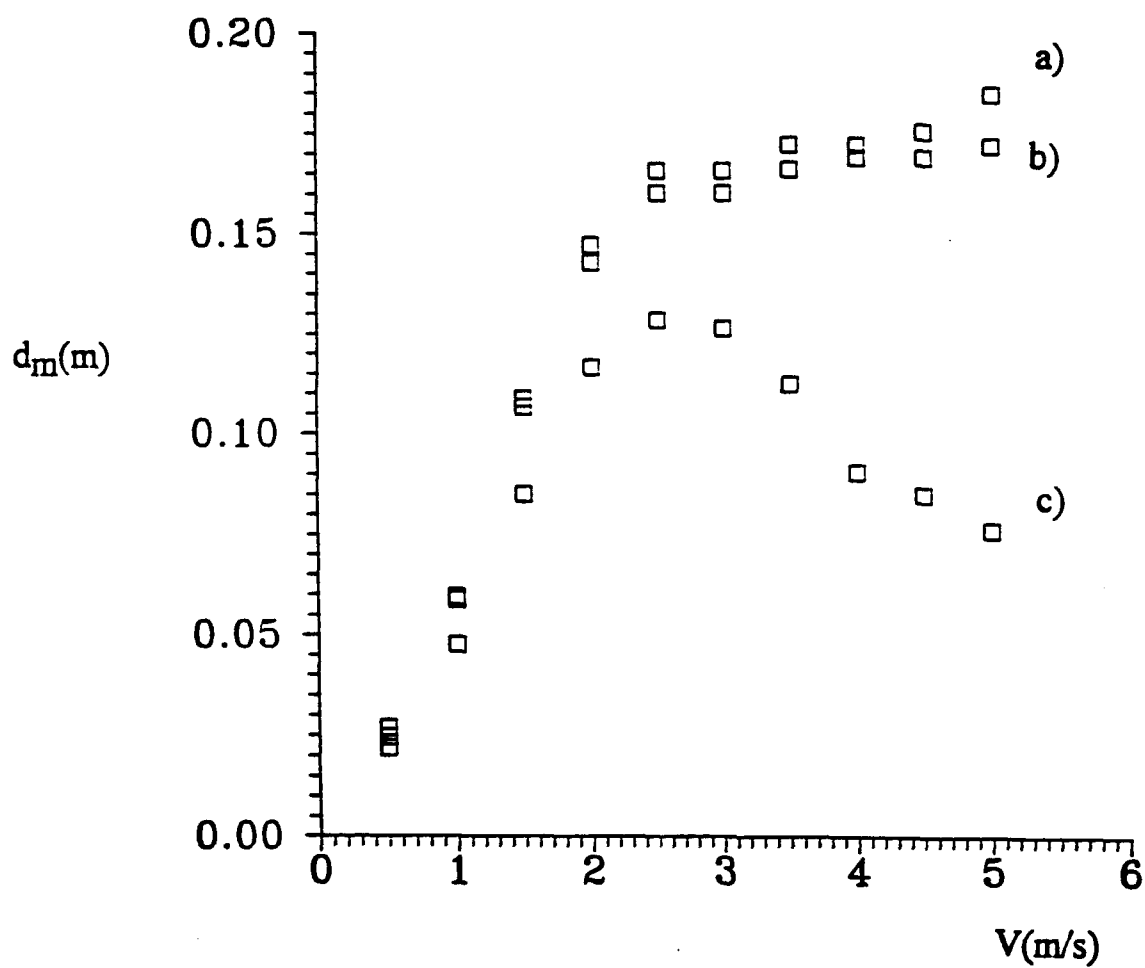


Figure 22 Maximum depth  $d_m$  as a function of the jet velocity for different initial positions:

a)  $y(t=0) = -h/2$

b)  $y(t=0) = 0$

c)  $y(t=0) = +h/2$



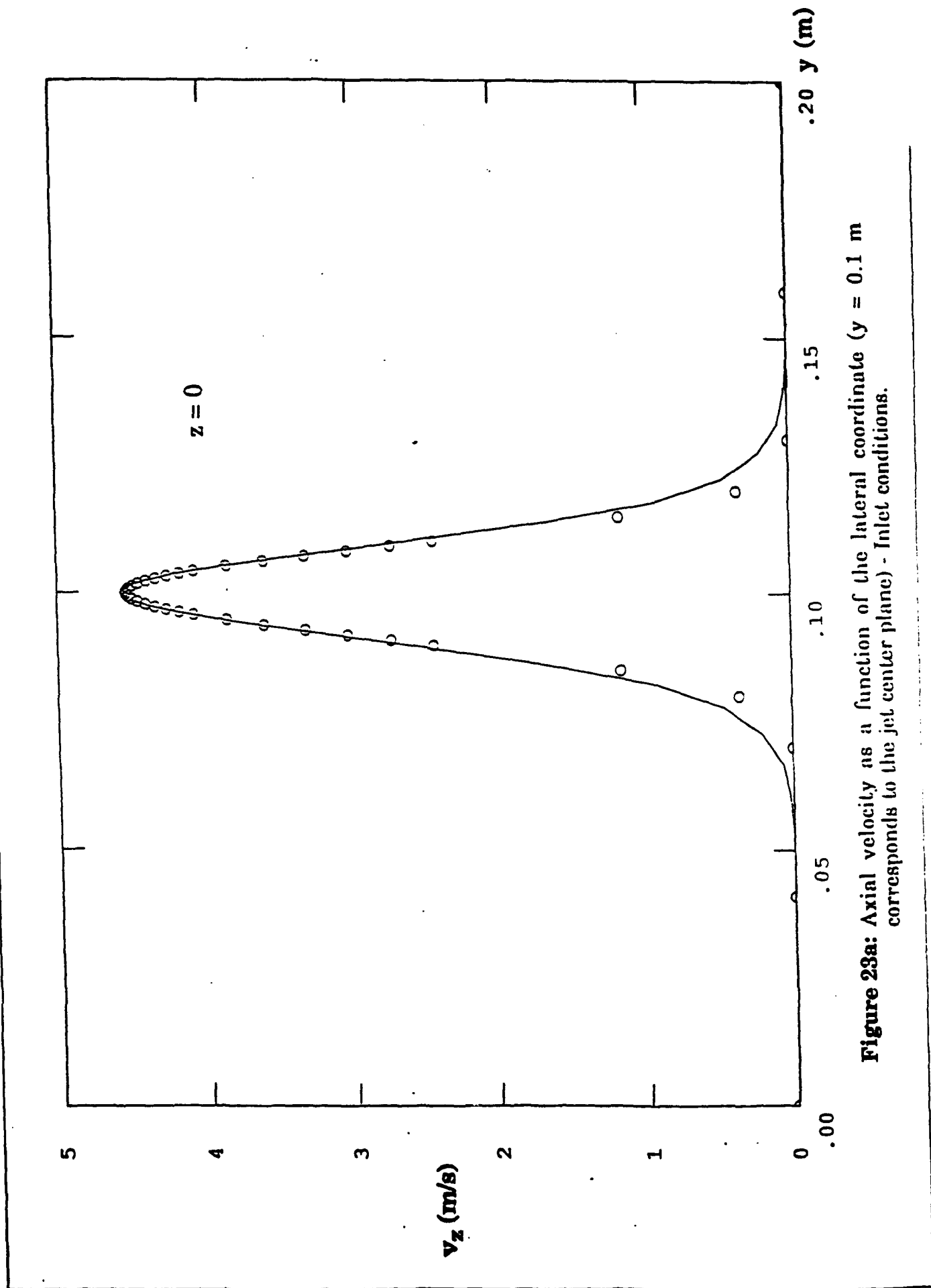


**Figure 23a:** Axial velocity as a function of the lateral coordinate ( $y = 0.1$  m corresponds to the jet center plane) - Inlet conditions.

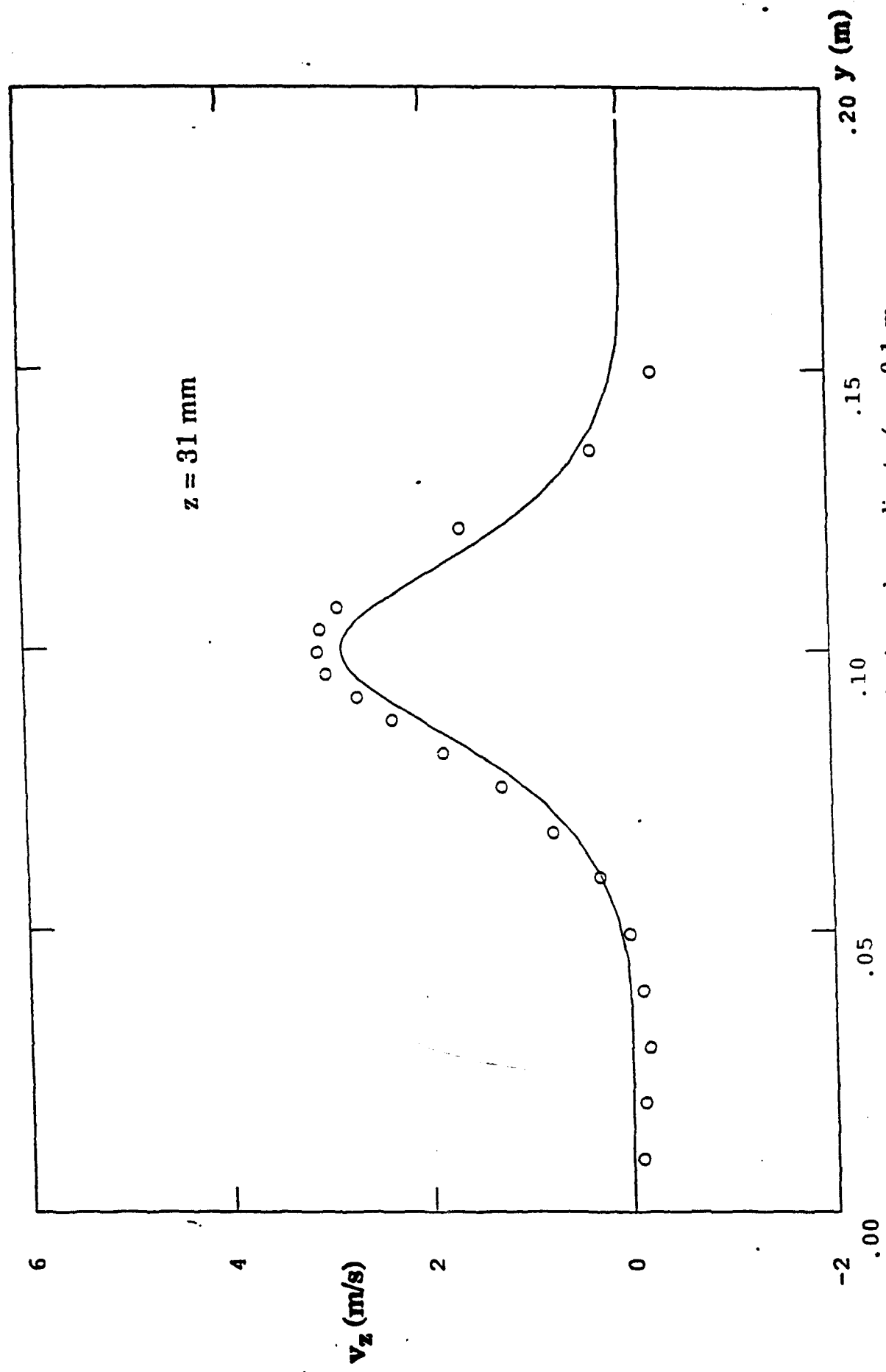


**Figure 23b:** Axial velocity as a function of the lateral coordinate ( $y = 0.1 \text{ m}$  corresponds to the jet center plane. The circles, O, are experimental results)

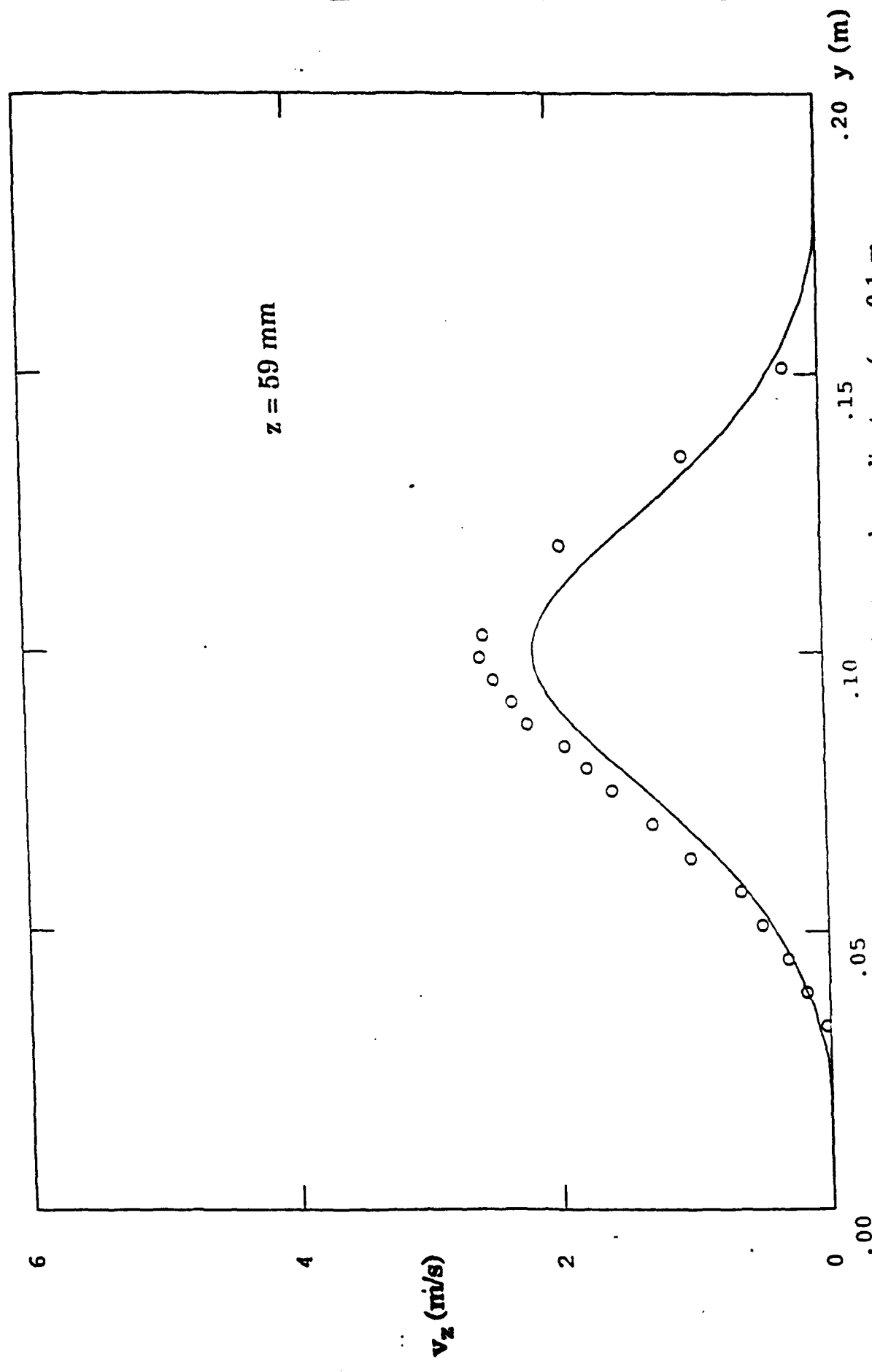


**Figure 23c:** Axial velocity as a function of the lateral coordinate. ( $y = 0.1$  m corresponds to the jet center plane. The circles,  $\circ$ , are experimental results)

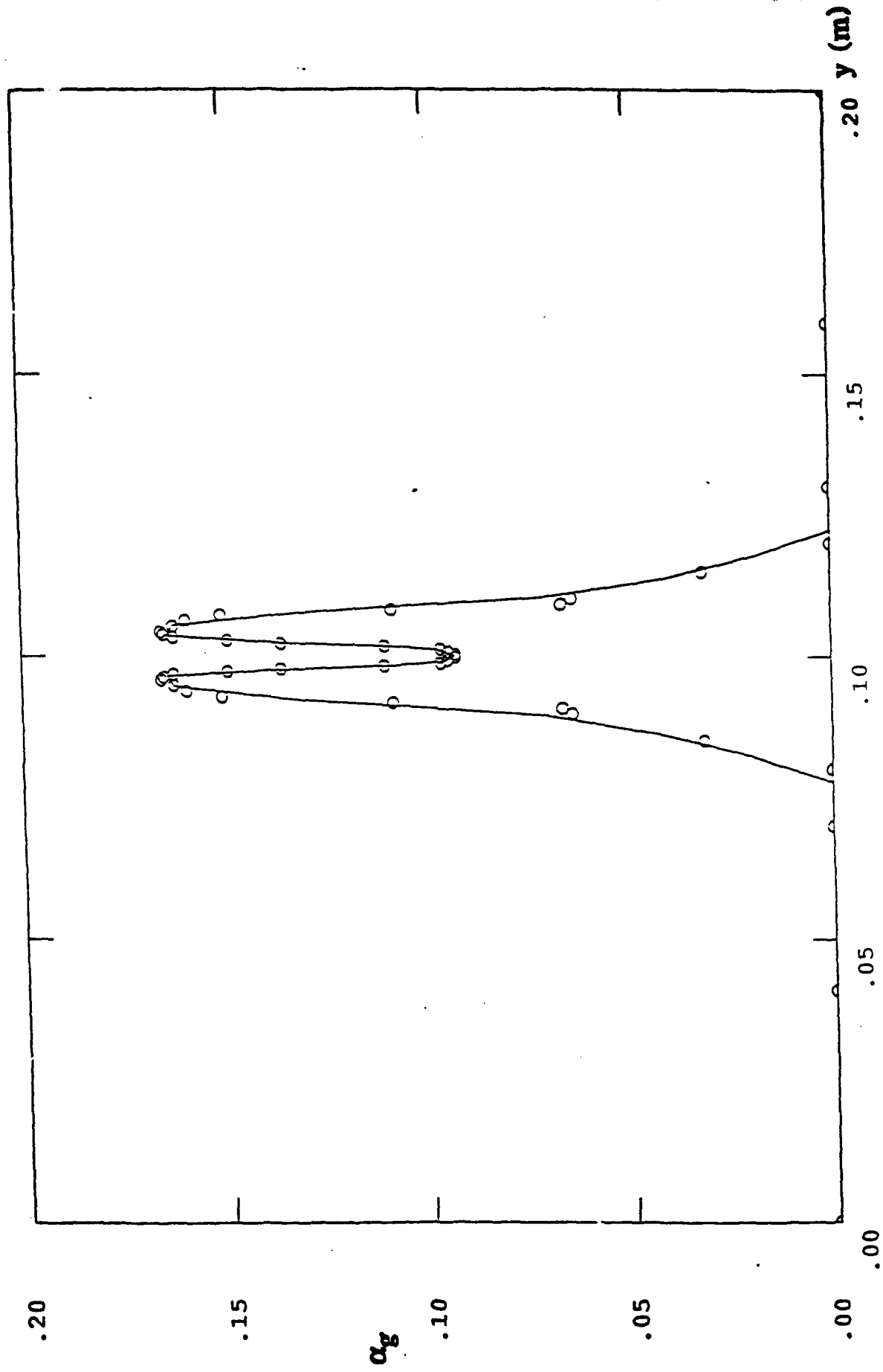


**Figure 24a:** Void fraction as a function of the lateral coordinate. ( $y = 0.1$  m corresponds to the jet center plane) - Inlet conditions

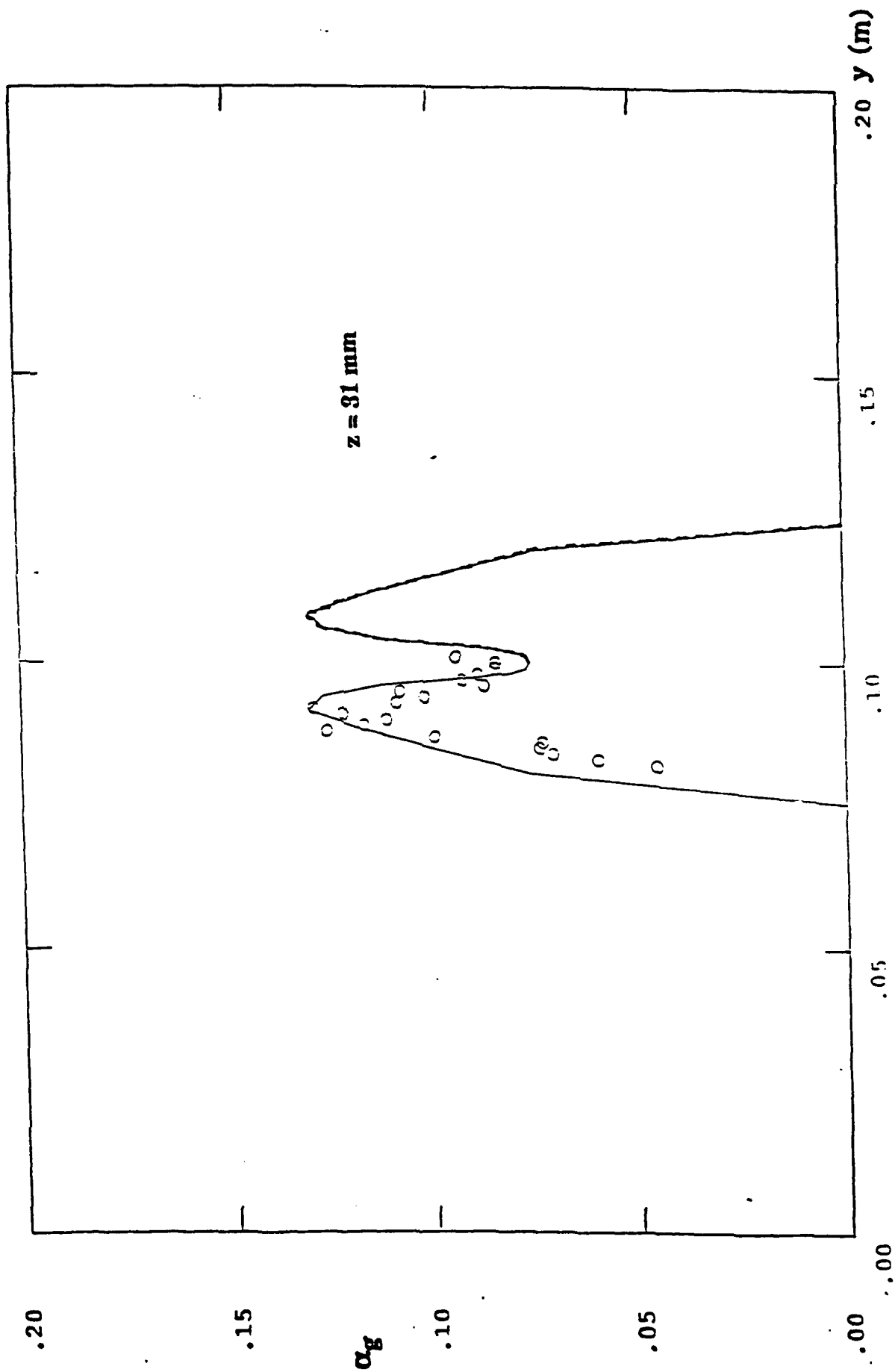


**Figure 24b:** Void fraction as a function of the lateral coordinate. ( $y = 0.1 \text{ m}$  corresponds to the jet center plane. The circles, o, are experimental results)

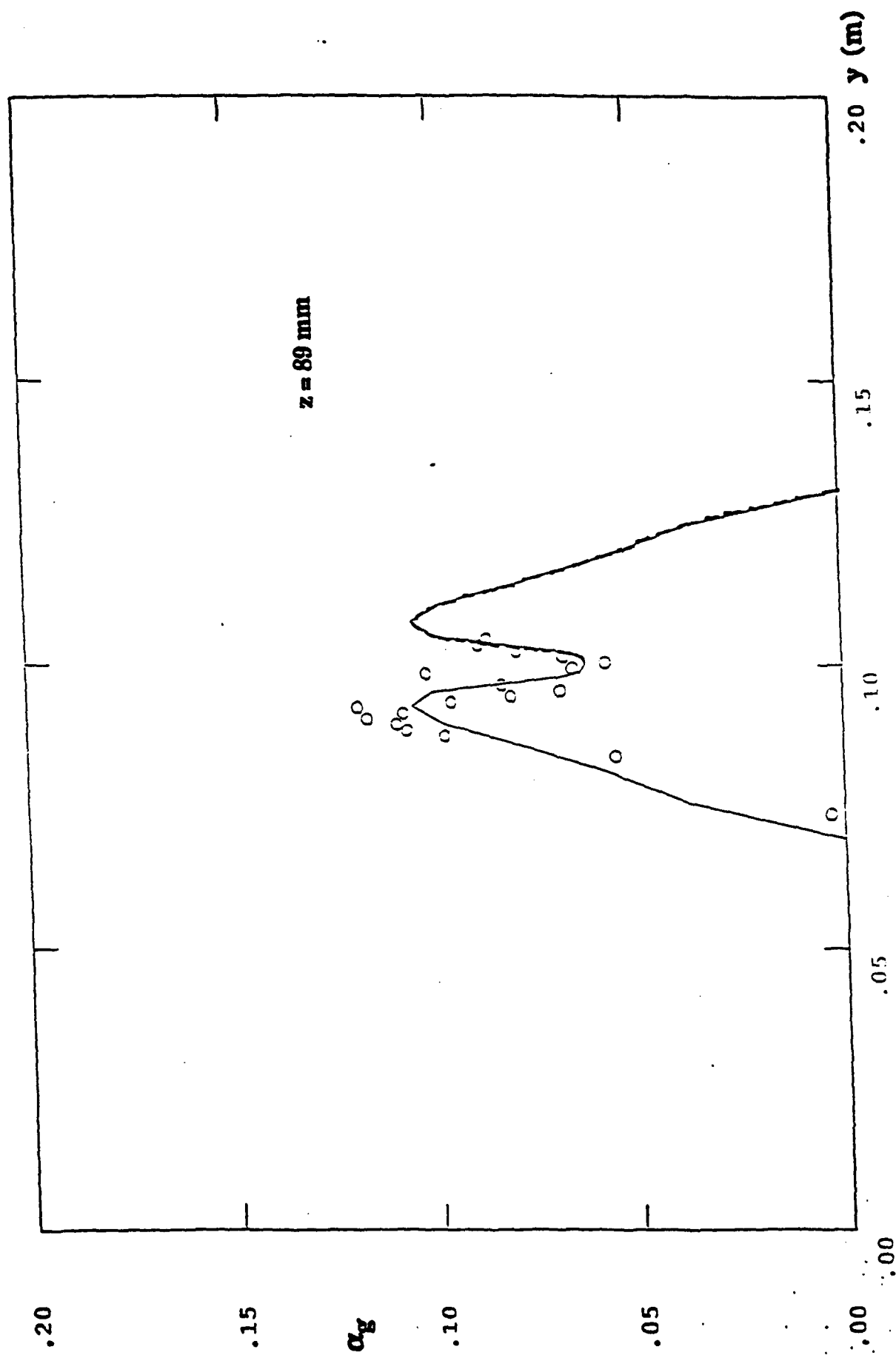


Figure 24c: Void fraction as a function of the lateral coordinate. ( $y = 0.1 \text{ m}$  corresponds to the jet center plane. The circles, o, are experimental results)

Figure 25 Schematics of the test section.

